frontiers | Frontiers in Earth Science

TYPE Original Research
PUBLISHED 17 April 2024
DOI 10.3389/feart.2024.1359617

OPEN ACCESS

EDITED BY
Paola Marianelli,
University of Pisa, Italy

REVIEWED BY
Weiqiang Li,
Nanjing University, China
Sylvestre Ganno,
University of Yaounde I, Cameroon

*CORRESPONDENCE
Mabrouk Sami,
mabrouksami@uaeu.ac.ae
Mohamed Faisal,
mohamed_faisal_89@science.suez.edu.eg
El Saeed R. Lasheen,
elsaeedlasheen@azhar.edu.eg

RECEIVED 21 December 2023
ACCEPTED 21 March 2024
PUBLISHED 17 April 2024

CITATION
Sami M, Faisal M, Leybourne M, Sanislav IV, Ahmed MS and Lasheen ESR (2024), Unravelling the genesis and depositional setting of Neoproterozoic banded iron formation from central Eastern Desert, Egypt. *Front. Earth Sci.* 12:1359617. doi: 10.3389/feart.2024.1359617

Unravelling the genesis and depositional setting of Neoproterozoic banded iron formation from central Eastern Desert, Egypt

Mabrouk Sami[1,2]*, Mohamed Faisal[3]*, Matthew Leybourne[4,5], Ioan V. Sanislav[6], Mohamed S. Ahmed[7] and El Saeed R. Lasheen[8]*

[1]Geosciences Department, College of Science, United Arab Emirates University, Al Ain, United Arab Emirates, [2]Geology Department, Faculty of Science, Minia University, El-Minia, Egypt, [3]Department of Geology, Faculty of Science, Suez Canal University, El-Ismailia, Egypt, [4]Department of Geological Sciences and Geological Engineering, Queen's University, Kingston, ON, Canada, [5]Department of Physics, Engineering Physics and Astronomy, Arthur B. McDonald Canadian Astroparticle Physics Research Institute, Queen's University, Kingston, ON, Canada, [6]Economic Geology Research Centre (EGRU), College of Science and Engineering, James Cook University, Townsville, QLD, Australia, [7]Geology and Geophysics Department, College of Science, King Saud University, Riyadh, Saudi Arabia, [8]Department of Geology, Faculty of Science, Al-Azhar University, Cairo, Egypt

The Neoproterozoic banded iron formations (BIFs) are widely occurred in the Egyptian Eastern Desert. This study integrates field observations, petrographic studies, geochemical data, and lead isotopes to construct the genesis and depositional environment of Wadi El-Mis hama BIF deposits. The iron layers, primarily of oxide facies within a volcano-sedimentary sequence, comprise magnetite-rich beds alternating with jaspilite or silicate laminae. The studied BIFs exhibit a dominant composition of SiO_2 and $Fe_2O_3{}^t$ with relatively low contents of TiO_2 and Al_2O_3. The positive correlation of REEs (La, Sm, Yb) with Zr and low concentrations of HFSEs (Ta, Nb, Th, Hf) indicate a primary formation mechanism of chemical precipitation, maintaining original geochemical signatures. Geochemical patterns show depletion in LREEs, enrichment in HREEs (La/Yb_{PAAS} = 0.08–0.12), and positive La anomalies (La/La_{PAAS} = 1.15–8.57), consistent with seawater influence. Additionally, various geochemical discrimination diagrams supported by elevated super-chondritic Y/Ho values (29.6–38.7), weak positive Eu anomalies, and low contents of transition metals (Cu and Zn), point to the interaction of low-temperature (<200°C) hydrothermal fluids (bearing Fe and Si) with seawater during the deposition of the BIFs. The lack of significant negative Ce anomalies along with low Ni/Co, U/Th, and Cu/Zn ratios, imply that the iron mineralization was precipitated from dysoxic to oxic conditions. The geochemical and Pb isotopic data suggest that the iron deposits formed in an extensional geodynamic setting (intra-oceanic arc basin environment) due to the subduction of the Mozambique Plate, with signatures closely matching other Precambrian Algoma-type BIFs.

KEYWORDS

banded iron formations, Algoma-type, Egyptian Eastern Desert, back-arc basin, Pb-isotopes

1 Introduction

Banded Iron-Formations (BIFs) are chemical sedimentary rocks characterized by finely laminated to thinly bedded layers, with alternating dark iron-rich and light silica-rich bands of various thicknesses, indicative of the changing oxidation state of the ocean and atmosphere (Frei et al., 2013). Although banding is a common feature in BIFs, it is not always completely preserved due to varying degrees of metamorphism and deformation (Bekker et al., 2010). BIFs, forming the world's predominant iron resource (over 95%) due to their global distribution, were mainly precipitated throughout the Archean and Paleo-Meso Proterozoic (~3.8 and 1.1 Ga) (Pirajno and Yu, 2021; Zhou et al., 2024), with subordinate BIFs deposited from the late Neoproterozoic (Cachoeirinha group, Borborema Province, NE Brazil) (Usma et al., 2021) to early Paleozoic (Taxkorgan Terrane, West Kunlun, China) (Ding et al., 2021). In comparison to the Archean and Paleoproterozoic BIFs, Neoproterozoic BIFs have simple geochemistry and are dominated by oxide facies, and were created in a more oxygenated environment (Cox et al., 2013) (Supplementary Table S1).

Based on the depositional environment, tectonic setting, and size, BIFs are commonly subdivided into three main types, namely Algoma-type, Superior-type, and Rapitan-type (Gross, 1980). The Algoma-type iron formations are comparatively small, stratigraphically associated with submarine volcanogenic successions (felsic to ultramafic rocks), and were likely deposited within extensional geodynamic regimes (deep-water conditions in association with hydrothermal fluids), particularly near spreading centers or in restricted basins (rifted island arcs and back-arc basins). They are characterized by high magnetite content and rapid changes in thickness (Supplementary Table S1). In some cases, they are associated with volcanogenic massive sulfide (VMS) deposits (Bekker et al., 2010). In contrast, the Superior-type is hundreds of meters thick and commonly associated with metasedimentary sequences (i.e., dolostone and shale) without direct relationships with volcanic rocks (Simonson, 1985). Superior-type BIFs were formed in relatively shallow marine conditions over large areas on continental shelves and slopes of passive margins or in intracratonic basins (for example, Australia Hamersley and South Africa Transvaal BIFs deposits) (Li et al., 2014; Pirajno and Yu, 2021). A third type is Rapitan-type, which has been linked to global glaciations (Snowball Earth events) and is distinguished by extreme climate changes and significantly higher atmospheric PO_2 (Planavsky et al., 2014). Significant deposits of this type are found in the Rapitan Group in northern Canada and the Urucum district of Brazil (Klein, 2005). Due to these variations from place to place, it has proved difficult to pinpoint a single depositional model that accurately depicts the formation of all BIFs.

Precambrian BIFs reveal important details about the evolutionary processes and the genesis of chemical sedimentary rocks deposited in marine environments (Isley and Abbott, 1999). It is mostly accepted that iron was generally scavenged from the early oceanic crust. The upwelling of ferrous iron (Fe^{2+}) from submarine hydrothermal vents, followed by oxidation into ferric iron (Fe^{3+}) in the upper levels and re-deposited on the ocean floor, is linked to most BIFs types (Polat and Frei, 2005). In addition, some recent studies (Li et al., 2015) indicated that continental Fe recycled by microbial dissimilatory iron reduction processes has also been proposed as an important source of Fe in BIFs. Globally, most BIFs have undergone significant diagenetic and metamorphic modifications after their formation (Klein and Beukes, 1993).

The Arabian–Nubian Shield (ANS) hosts several occurrences of BIFs (~fifteen localities, for example, Wadi Sawawin area in Saudi Arabia, Wadi El-Dabbah area in Egypt, Tambien Group in Ethiopia) (El-Habaak, 2021), which formed during the late Proterozoic and are classified as Algoma-type BIFs. Several small to moderate-size BIFs are recorded and preserved in Egyptian basement rocks (Figure 1; the northern part of the ANS) and accessible today for investigation and study, including: (a) Neoproterozoic BIFs in the Central Eastern Desert (Abu Marwat, Abu Rakib, Abu Diwan El Imra, Gebel El Hadid, El Hundusi, Gebel Semna, Fatira, Um Anab, Um Ghamis El Zarqa, Um Ghamis El Hamra, Um Lassaf, Um Nar, Um Shaddad, Sitra, Wadi El-Dabbah, Wadi Hamama, Wadi Kareim, and Wadi El-Mishama) (Basta et al., 2011; El-Shazly et al., 2019; El-Habaak, 2021) and the South Eastern Desert (scattered areas belonging to the Shadli Metavolcanics Belt) (Khudeir et al., 1988), and (b) Archean-Early Proterozoic BIFs exposed in South Western Desert (Uwaynat area) (Said et al., 1998), and southern Sinai (Wadi Madsus and El Samra area) (Khalid and Oweiss, 1997). Some localities are excluded from the BIF ore type due to the lack of aerial extent and economic potential.

The prospective area, Wadi El-Mishama (Figures 2, 3A), lies in the Central part of the Eastern Desert and includes Neoproterozoic BIFs, which were most likely formed during the island-arc stage of the Pan-African Orogeny (Stern and Hedge, 1985; Basta et al., 2011; El-Shazly et al., 2019; El-Habaak, 2021). No geological information or analytical data on the investigated area have yet been published elsewhere. In this contribution, the BIFs and their country rocks from Wadi El-Mishama were investigated. We report the first field observations, petrographic studies, and whole-rock geochemical and Pb isotope data. The aims of the present study are to: (a) constrain the origin of the Wadi El-Mishama BIFs, (b) identify the past geological processes/conditions under which the studied BIFs were precipitated, (c) characterize the Wadi El-Mishama BIFs by comparing them to other representatives Precambrian Algoma-type BIFs in the ANS and around the world, and (d) provide a deeper understanding of the evolution of the Eastern Desert in the Neoproterozoic era. Finally, the data presented here will guide further exploration studies to delineate the iron orebodies.

2 Geologic setting

2.1 Regional geology

The ANS in the north and the Mozambique Belt in the south are two separate parts of the East African Orogen. It was initiated around 900–870 Ma (Rodinia breakup) and ended around 620 Ma, when east and west Gondwana fragments collided and blocked the Mozambique ocean along the East African–Antarctic Orogen (Ali et al., 2023; Sami et al., 2023a; Sami et al., 2023b). The ANS continued with increasingly intense deformation during the Ediacaran (~630–550 Ma) as the result of the emplacement of large granitoids, and transtension, transpression, uplift, and

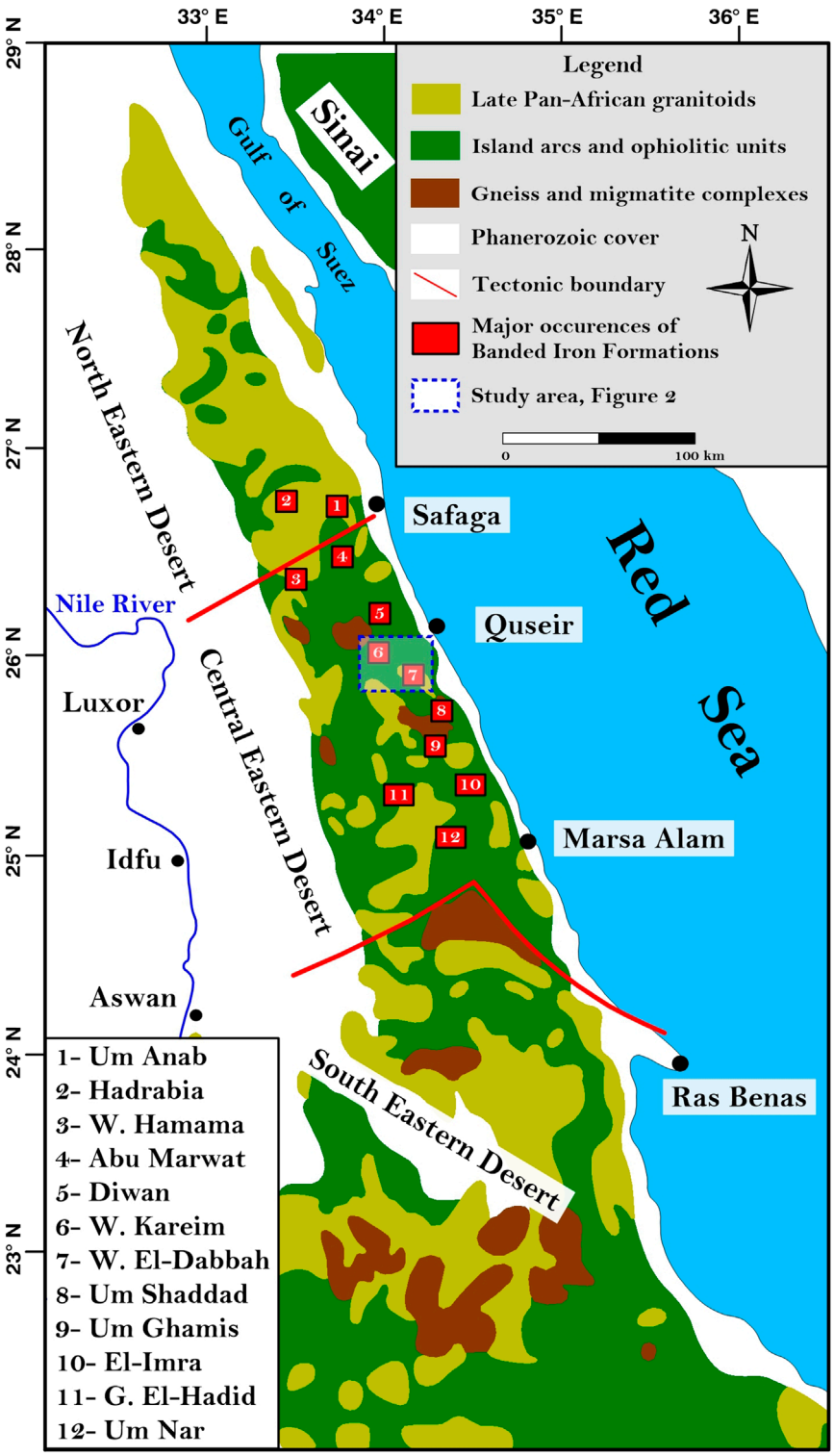

FIGURE 1
Geological map of the Eastern Desert of Egypt with the distribution of major Neoproterozoic Pan–African basement units and Banded Iron Formations [modified after Sami et al. (2020)]. The blue rectangle shows a more detailed map in this Figure. The solid red lines represent the boundaries between the northern, central, and southern parts of the Eastern Desert (Stern and Hedge, 1985).

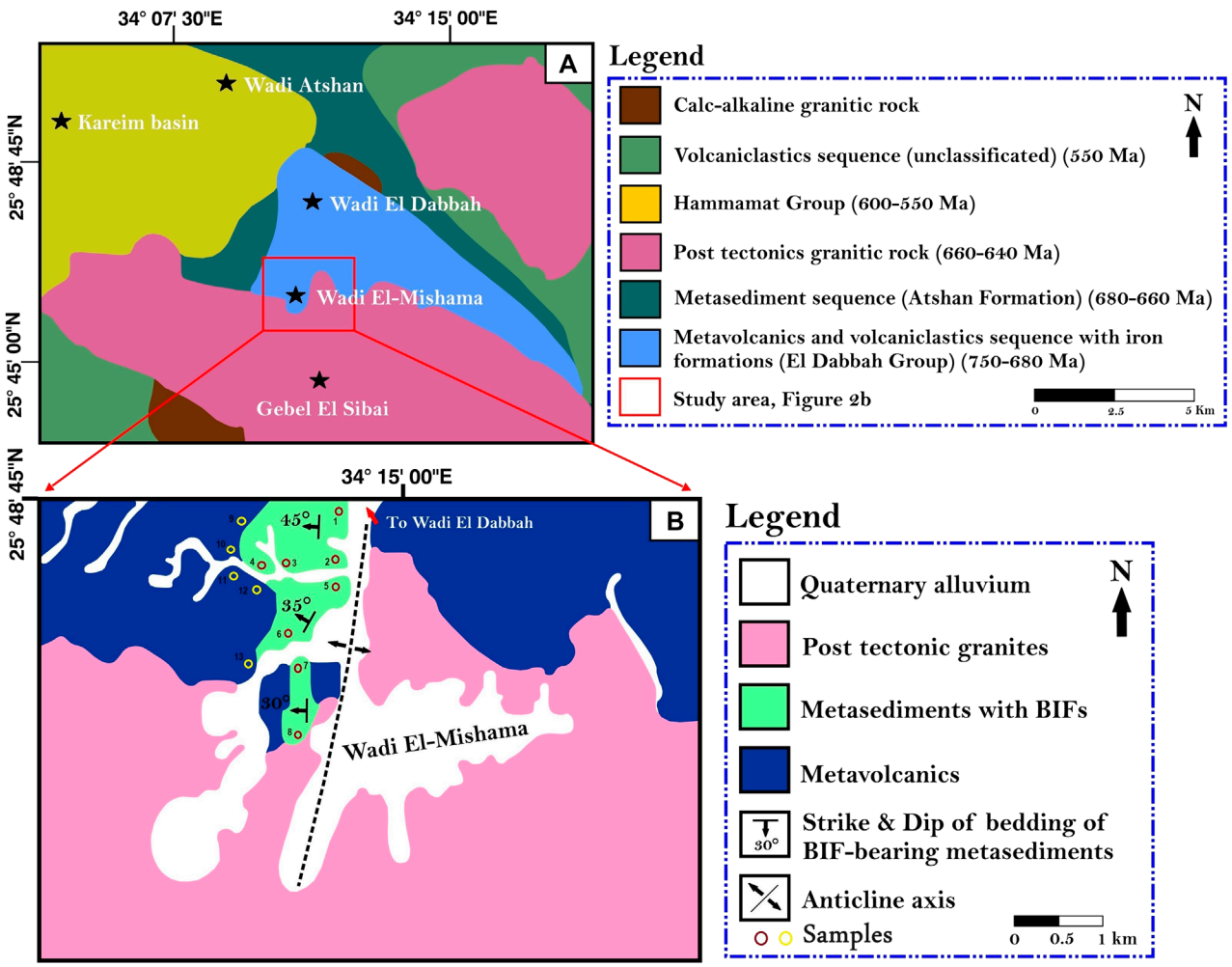

FIGURE 2
(A) Simplified geologic map of the study area, **(B)** Detailed view of the Wadi El-Mishama area.

exhumation associated with escape tectonics and orogenic collapse (Abd El Monsef et al., 2023; El-Dokouny et al., 2023). The ANS is a collage of high-grade metamorphic core complexes, late Proterozoic juvenile arcs, ophiolitic mélanges, voluminous granitoids, and pre-Neoproterozoic crust enclaves (Sami et al., 2022).

The basement complex of the Egyptian Eastern Desert is dominated by Neoproterozoic Island arcs and ophiolites (Figure 1), which are mostly found in the central and southern regions (Fawzy et al., 2020). The Central Eastern Desert (CED, ~800 km long) is made up of several thrust sheets, each produced at the base of dismembered ophiolites and capped by island-arc rock assemblages. These juvenile arcs (with variably well-preserved ophiolites) were formed in a subaqueous environment and are characterized by both forearc and back-arc geochemical signatures (Faisal et al., 2020). They are host to a diverse range of economically viable small to medium-sized metallic mineral resources (e.g., BIFs, VMS, orogenic gold). The CED basement rocks suffered regional deformation and metamorphism up to greenschist facies during the period of East African Orogen formation (Abdelfadil et al., 2022). These conditions ranged from 400°C ± 50°C, 4 ± 2 kbar in the northern part of the CED to 520°C ± 30°C, 5 ± 2 kbar in the southern part of the CED (El-Shazly and Khalil, 2016).

The BIFs, which are principally confined between latitudes 25°12′ and 26° 30′N, produced voluminous high-grade iron ores in some localities with ore reserves estimated at ~17.7, 13.7, and 11.1 Mt for Wadi Kareim, Um Nar, and Um Shaddad BIFs, respectively (El-Habaak, 2021). In terms of geotectonics, three depositional models have been applied to the BIFs in the CED of Egypt: (a) they were formed by chemical precipitation on a continental shelf with the source of iron being continental (El Aref et al., 1993); (b) they were likely originated by precipitation following low-temperature hydrothermal activity and submarine volcanism in an extensional geodynamic condition (i.e., an intra-back-arc basin setting) (El-Shazly et al., 2019) during Mozambique Ocean closure stage of the Pan-African Orogeny (~696 Ma) (Abd El-Rahman et al., 2019) (c) other authors attribute their formation to the concomitant melting of glacial ice during the Snowball Earth's interglacial period (~750 Ma) (Stern et al., 2013), which is

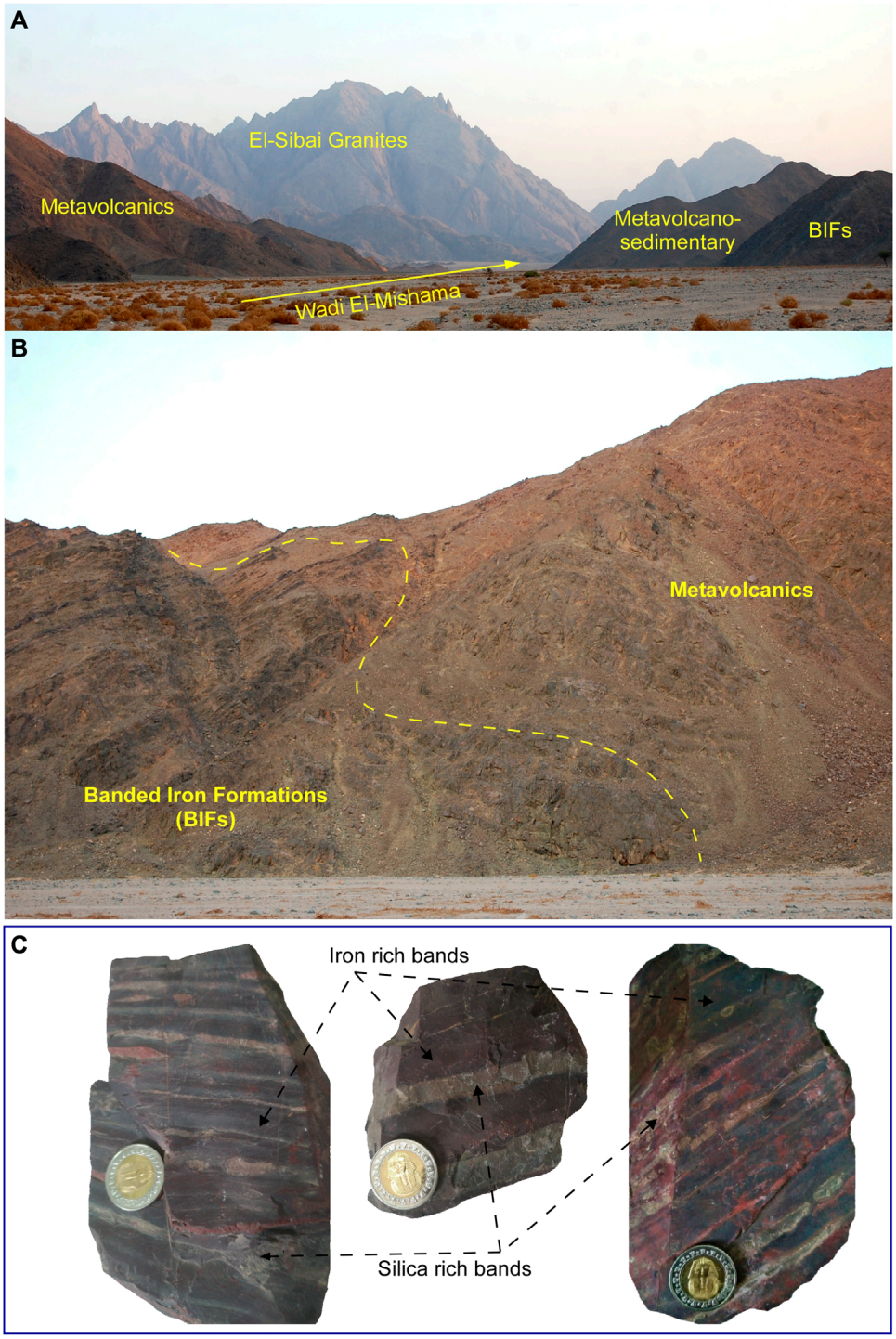

FIGURE 3
Field and hand specimen photographs of lithological units in the Wadi El-Mishama area showing: **(A)** Entrance of Wadi El-Mishama and outcrop of iron ore sequence, looking S, **(B)** General overview showing the occurrence of layered BIFs with the metavolcanics, **(C)** Close-up view of a sample chip from the red jasper and hematite-rich iron sequence.

supported by the existence of small diamictite beds within the volcaniclastic successions (i.e., Wadi Kareim, Wadi Mobark, and Nuwaybah formations) (El-Shazly and Khalil, 2016). The majority of Egyptian BIFs are poorly constrained in terms of extent, grade, and tonnage, and in terms of tectonic, metamorphic, geochemical, and geochronological characteristics.

2.2 Deposit geology

The study area, Wadi El-Mishama, is located in the middle segment of the Eastern Desert (south of the Wadi El-Dabbah area, Figure 2). Wadi El-Mishama belongs to the Lower El-Dabbah Formation (total thickness of ~2 km) that consists mainly of a metavolcano-sedimentary sequence and is overlain by subaerial sedimentary rocks (the Hammamat Group and Atshan Formation; Figure 3A). Three stratigraphic units are identified within the study area (i.e., arc-related volcanic flows, BIF-rich volcaniclastic rocks, and tuff-rich volcaniclastic rocks). The low-grade island-arc assemblages are commonly represented by massive pillow basaltic flows interlayered with a thin volcaniclastic sequence. In the upper part of this formation, pale greenish volcanic tuff along with several thin beds of well-preserved iron sequences (several meters thick) are observed. This succession contains well-preserved volcano-sedimentary structures including pillow lava, graded and parallel laminated tuffs, and iron oxide layers (Figure 3). Furthermore, the tuff-rich volcaniclastic layers display slumping, folding, and faulting features, indicating that these strata experienced syn-to post-depositional deformation.

2.3 Field observations and petrography

The BIF occurrences within the study area are notably significant, presenting several meters in thickness, which is indicative of extensive iron deposition events within the volcaniclastic rocks (Figure 3B). These BIF layers are characterized by their well-defined banding, alternating between iron-rich layers and silica-rich bands, reflecting periodic conditions of deposition (Figure 3C). The BIF outcrops exhibit varying sizes, with some extending several tens of meters in length and width and grade of these BIFs varies, with iron content significantly influencing the economic value of these deposits.

Microscopic analysis shows that the studied felsic lavas are mainly composed of feldspar and quartz. Euhedral magnetite is observed as fine-grained disseminations within these rock units (Figure 4). The well-exposed BIF (magnetite-rich beds alternating with jaspilites or silicate laminae) from the Wadi El-Mishama area is an example of Neoproterozoic oxide-facies BIFs in the ANS. They are commonly found at different scales, ranging from a few centimeters to as much as several meters thick. At the microscopic scale, the BIF layers are composed of alternating quartz-rich light and magnetite-rich dark microbands (Figures 4A, B). Magnetite and hematite are the common Fe-minerals in the studied BIFs (Figures 4C, D). Additionally, there are clearly developed and preserved sedimentary structures (i.e., bedding and graded bedding). The studied units are bounded by a strongly foliated metasedimentary sequence and are in intrusive contact with granitoids (hornblende–biotite granite) (Kiyokawa et al., 2020). The entire sequence experienced greenschist-facies metamorphism with brittle deformation and minor brittle-ductile deformation (i.e., pressure-temperature conditions of 373°C ± 61°C and 1.1–2.2 kbar) (El-Shazly and Khalil, 2016).

3 Investigative methodologies

3.1 Samples collection and preparation

A total of sixty (60) representative samples from BIFs and their host rocks distributed over the Wadi El-Mishama area were collected during two field trips. The location of the samples was highly dependent on the availability and accessibility of outcrops. The collected samples are massive, homogeneous, and least weathered, and were carefully selected based on color, texture, and macro-scale mineralogy variations. Twenty-five (25) samples were cut and polished to prepare thin and polished sections for carrying out systematic microscopic descriptions. Based on the detailed microscopic investigation, thirteen (13) samples were selected for whole rock chemical analysis, including eight (8) samples from BIFs and five (5) samples from metavolcanic wall rocks. These samples were also chosen for further analyses, that is, lead isotope analysis.

3.2 Analytical methods

Analyses performed at ALS Geochemistry, North Vancouver, British Columbia, Canada included the following: 1) major elements were analyzed by ICP-AES following lithium metaborate fusion; 2) trace elements (Ba, Cr, Cs, Ga, Hf, Nb, Rb, Sr, Ta, Th, U, V, Y, Zr, and the REE) by ICP-MS following lithium metaborate fusion (method ME-MS81); and 3) trace and some major elements (Ag, Al, As, Ba, Be, Bi, Ca, Cd, Ce, Co, Cr, Cs, Cu, Fe, Ga, Ge, Hf, In, K, La, Li, Mg, Mn, Mo, Na, Nb, Ni, P, Pb, Rb, Re, S, Sb, Sc, Se, Sn, Sr, Ta, Te, Ti, Tl, U, V, W, Y, Zn, Zr) by an ultra-trace four-acid digestion (HF, $HClO_4$, HCl, HNO_3) method (method ME-MS61L) followed by a mixture of ICP-AES and ICP-MS analysis. Data quality was monitored through the use of the following certified reference materials: OREAS-101b, 920, 47, 45e, and 14p; SY-4; BCS-512; AMIS0167, 0085, 0304. The REE anomalies of BIF samples were calculated as: $Ce/Ce* = [(Ce_{PAAS}/(La_{PAAS} \times Pr_{PAAS})1/2]$; $Pr/Pr* = [Pr_{PAAS}/(Ce_{PAAS} \times Nd_{PAAS})1/2]$; $Eu/Eu* = [Eu_{PAAS}/(Sm_{PAAS} \times Gd_{PAAS})1/2]$; $La/La* = [(La_{PAAS})/(3 \times Pr_{PAAS}) -(2 \times Ho_{PAAS})]$ (Bolhar et al., 2004).

Lead isotopes were measured on a quadrupole ICP-MS at ALS Geochemistry following four acid digestion of whole rock powders (method MS61L-PbIS). Procedural blanks for most elements are less than the detection limits. For the Pb isotopes, procedural blanks are typically <0.01 ppm. Precision and accuracy of the Pb isotope results are typically 0.5%–3%, and for major and trace elements typically <5%.

For the major and trace elements a variety of certified reference materials (CRMs) were used including SY-4, BCS-512, AMIS0571, CDN-W-4, OREAS 920, OREAS-101b, AMIS0547, AMIS0167, AMIS0085, AMIS0304, OREAS 146, OREAS-14P, AMIS0461, OREAS 47, OREAS-45e. For the Pb isotopes, certified reference materials OREAS 920, 47, and 45e were analyzed concurrently. All CRM data is available on request.

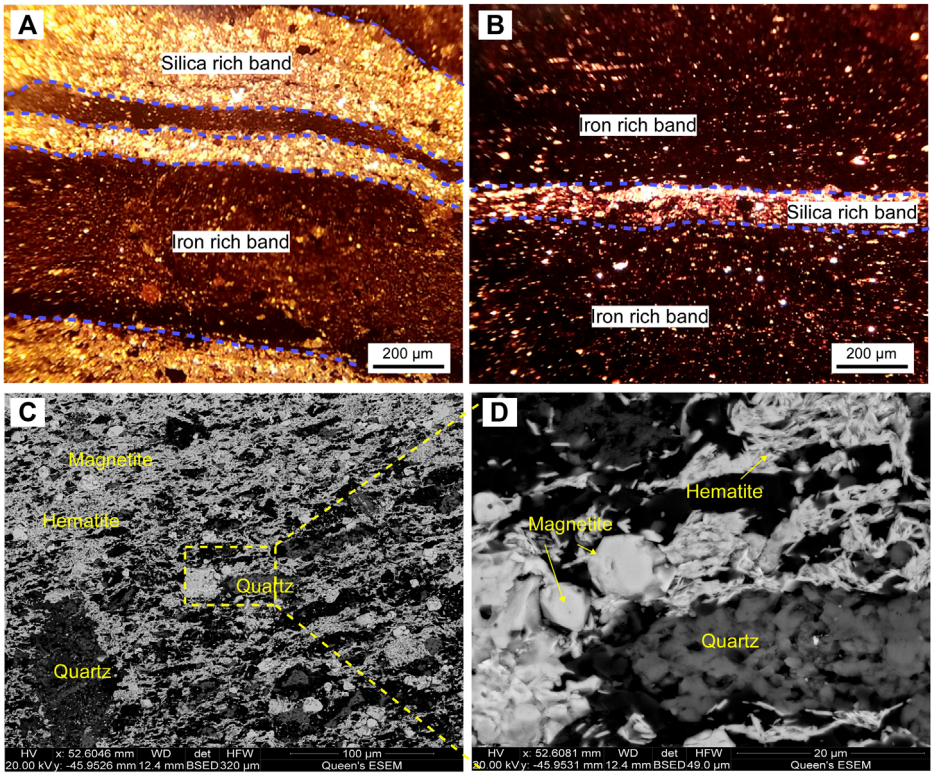

FIGURE 4
Photomicrographs and BSE images showing the representative mineral assemblages: **(A,B)** BIFs comprising iron oxide rich alternating with silicate rich bands; **(C,D)** BSE images shows the distribution of iron oxides (mainly magnetite crystals) within the gangue minerals (i.e., quartz and feldspar minerals).

4 Results

4.1 Whole rock geochemistry

4.1.1 BIFs

Major oxides, trace, and rare earth elements (REEs) of the analyzed samples from the Wadi El-Mishama iron deposits, combined with relevant geochemical parameters, are presented in Table 1. Whole-rock chemical analyses of BIFs compiled from previous studies of the ANS (Khalil et al., 2015; Abd El-Rahman et al., 2019; El-Shazly et al., 2019) (Supplementary Table S2), are used to discuss the depositional environment and origin of the studied BIFs.

The $Fe_2O_3^t$ contents in the BIF samples range between 50.1 and 74.1 wt%, whereas the SiO_2 and CaO values vary from 26.6 to 34.4 wt% and from 1.3 to 7.7 wt%, respectively. The efficient removal of SiO_2, CaO, and MgO is responsible for the marked enrichment of iron in all ore samples (Gutzmer et al., 2008). Notably, all analyzed ore samples have significantly low concentrations of TiO_2 (0.08–0.2 wt%), Al_2O_3 (1.4–3.7 wt%), Na_2O (0.06–0.6 wt%), K_2O (0.07–0.3 wt%), MnO (0.03–0.05 wt%), and P_2O_5 (0.12–0.21 wt%, Table 1). On Harker diagrams (Figures 5, 6), the $Fe_2O_3^t$ correlates negatively with SiO_2, CaO, Al_2O_3, P_2O_5, Cr, and Zr. There is no significant difference in major element contents between the Wadi El-Mishama BIFs and the Eastern Desert Algoma-type BIFs in the ANS (Figures 5, 6). The BIF samples reveal wide variations of Mn (182–336 ppm), Cr (20.5–118.5 ppm), Ni (9.8–61.3 ppm), and Sr (28.6–92.4 ppm) concentrations (Table 1). Furthermore, the contents of Zr (16–53 ppm), Hf (0.5–1.6 ppm), Cu (3.27–16.05 ppm), and Zn (7.8–25 ppm), are low in general. During hydrothermal, diagenetic, and weathering processes, aluminum and titanium are thought to be largely immobile (MacLean and Kranidiotis, 1987). Here, Al_2O_3 contents show an inverse relation with $Fe_2O_3^T$ contents (Figure 5). In addition, during diagenesis, alumina-poor iron silicate minerals break down into iron hydroxide minerals and amorphous silica; as a result, chert bands are commonly formed where silica is trapped by iron oxide laminae. The SiO_2- $Fe_2O_3^t$ biplot (Figure 5) shows a declining trend of SiO_2 with rising Fe_2O_3 values, displaying the presence of a hematite-rich component with small chert micro-bandings in some samples.

In the primitive mantle (PM) normalized trace element diagram, BIFs exhibit negative Ti, Sr, Nb, and Pr anomalies (Figure 7A). The total REEs (ΣREE) concentration varies between 56.00 and 75.85 ppm (Table 1). The studied samples are characterized by depletion of light REE relative to heavy REE (La/Yb_{PAAS} = 0.08–0.12) (Figure 7B). The studied BIFs show obviously weak positive Eu_{PAAS} anomalies (Eu/Eu ∗ = 0.88–1.11, except for two samples with values of 0.67 and 0.73) and weak negative or no Ce_{PAAS} anomalies (Ce/Ce ∗ = 0.83–0.93) (Table 1; Figure 7B). In addition, most of the BIF samples have strong positive La_{PAAS} anomalies (La/La ∗ = 1.15–8.57). Compared to a chondritic Y/Ho value, the studied deposit has relatively high Y/Ho values (29.55–38.66, Table 1).

TABLE 1 Whole rock geochemical data from Wadi El-Mishama BIFs deposit (Central Eastern Desert, Egypt) for iron ore and wall rocks.

Facies	BIFs (Oxide Facies)								Metavolcanic rocks associated with the BIFs					Algoma-type	Superior-type	Rapitan-type
Sample Number	WM-1	WM-2	WM-3	WM-4	WM-5	WM-6	WM-7	WM-8	WM-9	WM-10	WM-11	WM-12	WM-13			
Major oxides (wt.%)																
SiO2	34.40	29.40	26.60	19.20	31.20	29.70	31.30	29.90	45.80	61.70	60.00	51.50	65.00	48.90	47.10	45.41
TiO2	0.20	0.16	0.13	0.10	0.08	0.10	0.18	0.16	0.43	0.26	0.46	0.38	0.48	0.12	0.04	0.08
Al2O3	2.74	3.65	2.31	2.28	1.38	2.38	3.42	3.39	9.46	10.10	10.90	10.15	11.35	3.70	1.50	0.49
Fe2O3T	54.90	50.10	64.10	74.10	55.50	58.40	52.50	52.00	7.20	6.52	10.65	7.75	4.71	39.70	40.30	44.46
MnO	0.04	0.05	0.04	0.04	0.03	0.04	0.05	0.05	0.19	0.10	0.08	0.14	0.08	0.25	0.65	0.08
MgO	0.95	1.29	1.12	1.28	0.64	1.08	1.12	1.06	1.64	1.55	2.37	1.93	1.42	2.00	1.93	0.43
CaO	3.41	7.69	3.27	1.26	6.03	5.29	7.64	7.08	17.80	8.70	6.38	14.25	8.03	1.87	2.24	4.38
Na2O	0.62	0.53	0.13	0.07	0.09	0.06	0.58	0.53	0.13	0.14	1.44	0.99	1.12	0.43	0.13	0.03
K2O	0.12	0.30	0.07	0.25	0.15	0.16	0.23	0.26	2.38	2.62	1.73	1.90	2.22	0.62	0.20	0.03
P2O5	1.20	1.55	0.97	0.71	2.35	2.01	1.54	1.43	2.39	1.19	1.80	1.34	0.42	0.23	0.08	0.91
Cr2O3	0.01	0.01	0.01	0.01	0.01	0.01	0.01	0.01	0.01	0.01	0.01	0.01	0.01	0.02	0.02	0.03
LOI	1.29	4.96	2.23	1.10	2.76	2.68	2.16	4.63	12.20	6.42	4.90	11.20	6.15	-	-	-
Total	99.88	99.69	100.98	100.40	100.22	101.91	100.73	100.50	99.63	99.31	100.72	101.54	100.99			
Al (wt.%)	1.45	1.93	1.22	1.21	0.73	1.26	1.81	1.79	5.01	5.34	5.77	5.37	6.01	1.96	0.79	1.79
Fe (wt.%)	38.40	35.04	44.83	51.83	38.82	40.85	36.72	36.37	5.04	4.56	7.45	5.42	3.29	17.41	19.72	29.02
Mn (wt.%)	0.03	0.04	0.03	0.03	0.02	0.03	0.04	0.04	0.15	0.08	0.06	0.11	0.06	0.19	0.49	0.08
Ca (wt.%)	2.44	5.50	2.34	0.90	4.31	3.78	5.46	5.06	12.72	6.22	4.56	10.18	5.74	1.27	1.60	1.64
Na (wt.%)	0.46	0.39	0.10	0.05	0.07	0.04	0.43	0.39	0.10	0.10	1.07	0.73	0.83	0.31	0.10	0.14
K (wt.%)	0.10	0.25	0.06	0.21	0.12	0.13	0.19	0.22	1.98	2.17	1.44	1.58	1.84	0.43	0.17	0.41

(Continued on the following page)

10.3389/feart.2024.1359617

TABLE 1 (*Continued*) Whole rock geochemical data from Wadi El-Mishama BIFs deposit (Central Eastern Desert, Egypt) for iron ore and wall rocks.

Facies	BIFs (Oxide Facies)								Metavolcanic rocks associated with the BIFs					Algoma-type	Superior-type	Rapitan-type
Sample Number	WM-1	WM-2	WM-3	WM-4	WM-5	WM-6	WM-7	WM-8	WM-9	WM-10	WM-11	WM-12	WM-13			
Fe/Ti	320.26	365.32	575.28	864.53	809.40	681.36	340.29	379.18	19.54	29.26	27.01	23.79	11.45	140.40	505.60	168.00
Al/(Al+Fe+Mn)	0.04	0.05	0.03	0.02	0.02	0.03	0.05	0.05	0.49	0.54	0.43	0.49	0.64	0.09	0.03	0.05
Base and precious metals (ppm)																
Cu	11.6	7.75	9.96	3.27	10.7	16.05	7.76	8.78	41.4	20.7	18.85	15.05	27.3	96	10	
Pb	3.03	2.36	2.16	1.44	1.94	1.55	1.4	2.69	4.5	2.75	3.22	3.7	2.77			
Zn	19.5	25	12.7	13.5	7.8	13.6	9.7	21.7	62.5	58.1	72.9	58.7	41.3	33	2	
Mn	264	298	210	209	198	260	182	336	1375	751	597	1110	646			
Ag	0.174	0.159	0.052	0.149	0.111	0.087	0.083	0.109	0.196	0.155	0.251	0.179	0.12			
Ni	40.1	25.7	26.5	9.8	42.7	36.6	61.3	22.9	26.3	182.5	54.6	27.6	108.5	83	32	
Cr	76.3	45.5	54.1	20.5	86.2	70.2	118.5	40.6	45.1	307	89.2	43.3	176	78	122	
Co	6.72	7.17	4.63	3.25	4.9	7.1	4.74	6.09	8.6	11.35	15.65	13	35.1	38	27	
Mo	2.35	2.15	1.73	2.07	3.57	2.85	3.66	2.34	1.22	5.02	1.46	0.81	2.56			
Trace elements (ppm)																
As	4.95	7.14	6.93	6.97	12.2	10.1	10.55	6.93	2.6	1.43	1.38	1.23	0.67			
Ba	36	57	16	63	45	50	44	45	316	345	286	324	440	170	180	
Be	0.38	0.51	0.57	0.63	0.44	0.46	0.46	0.52	0.6	0.56	0.8	0.75	0.87			
Bi	0.058	0.032	0.033	0.022	0.02	0.024	0.019	0.034	0.049	0.015	0.047	0.04	0.043			
Cd	0.04	0.075	0.024	0.027	0.041	0.044	0.029	0.079	0.416	0.284	0.156	0.398	0.63			
Cs	0.15	0.25	0.15	0.15	0.15	0.17	0.15	0.26	1.14	1.06	1.14	1.54	1.82			
Ga	3.82	5.04	2.96	3.05	1.77	2.81	1.98	4.53	10.75	11.85	13.55	12.75	12.85			
Ge	0.31	0.27	0.34	0.4	0.31	0.3	0.33	0.27	0.11	0.1	0.13	0.1	0.09			

(Continued on the following page)

10.3389/feart.2024.1359617

TABLE 1 (*Continued*) Whole rock geochemical data from Wadi El-Mishama BIFs deposit (Central Eastern Desert, Egypt) for iron ore and wall rocks.

Facies	BIFs (Oxide Facies)								Metavolcanic rocks associated with the BIFs					Algoma-type	Superior-type	Rapitan-type
Sample Number	WM-1	WM-2	WM-3	WM-4	WM-5	WM-6	WM-7	WM-8	WM-9	WM-10	WM-11	WM-12	WM-13			
Nb	1.9	1.6	1.3	1	0.7	0.8	0.9	1.5	4.1	3.1	4.5	3.8	4.8			
Hf	1.6	1.3	0.7	0.6	0.5	0.5	0.5	1.3	3.9	3.9	4.4	3.9	4.1			
Li	11.2	17.8	13.4	11.6	7.7	13.4	9.6	15.6	8.4	7.1	27.1	20.1	11.5			
In	0.018	0.021	0.018	0.012	0.01	0.013	0.011	0.021	0.062	0.053	0.058	0.055	0.06			
Sb	0.4	0.4	0.78	0.62	0.68	0.61	0.66	0.4	0.19	0.21	0.07	0.06	0.15			
Sc	6.43	6.07	5.47	5.75	4.37	4.58	4.37	5.99	13.05	8.73	13	12.1	14.45			
Se	3.47	0.574	0.858	0.174	0.546	0.587	0.442	0.767	3.49	1.07	0.829	0.887	1.35			
Sn	0.53	0.41	0.28	0.28	0.18	0.23	0.21	0.46	1.37	1.46	1.41	1.28	1.52			
Sr	81.7	92.4	33.5	29.2	39.2	45.2	28.6	90.5	185	131.5	134	167.5	187	98	42	
Re	0.0013	0.0011	0.0012	0.0008	0.0014	0.0019	0.0013	0.001	0.0023	0.0027	0.0019	0.0016	0.0051			
Rb	3.87	8.24	2.09	5.64	3.01	3.75	3.05	6.18	64.9	66.5	50.8	61.8	69.6			
Ta	0.2	0.1	0.1	0.1	0.1	0.1	0.1	0.2	0.4	0.2	0.3	0.3	0.3			
Te	0.198	0.035	0.075	0.028	0.04	0.045	0.044	0.047	0.126	0.021	0.028	0.031	0.034			
Tl	0.02	0.043	0.011	0.046	0.019	0.02	0.021	0.034	0.325	0.337	0.247	0.322	0.351			
Th	0.94	0.7	0.47	0.36	0.27	0.37	0.3	0.75	2.89	2.01	2.87	2.66	2.95			
U	0.15	0.14	0.07	0.06	0.1	0.1	0.07	0.14	3.34	1.18	1.1	1.2	1.16			
W	47	36.3	35.8	24.1	48.7	61.9	41.3	30.4	35	47.2	53.4	38.9	189			
V	49.4	42	50.9	54	39	42.8	41.3	42.1	31.9	33.2	61.8	65.5	61.2	97	30	
Y	22.4	25.9	24.5	19.5	32	24.2	26.4	24.2	47.9	27	43.9	35.1	30.1	54	41	
Zr	53	42	27	23	16	20	18	43	129	126	141	126	135	84	5	

(Continued on the following page)

10.3389/feart.2024.1359617

TABLE 1 (*Continued*) Whole rock geochemical data from Wadi El-Mishama BIFs deposit (Central Eastern Desert, Egypt) for iron ore and wall rocks.

Facies	BIFs (Oxide Facies)								Metavolcanic rocks associated with the BIFs					Algoma-type	Superior-type	Rapitan-type
Sample Number	WM-1	WM-2	WM-3	WM-4	WM-5	WM-6	WM-7	WM-8	WM-9	WM-10	WM-11	WM-12	WM-13			
Rare earth elements (ppm)																
La	4.1	4.3	4.1	3.5	3.5	3.8	3	3.9	17	11	17.3	15.7	12.8			
Ce	10.4	10.1	10.8	8	9.1	9.7	7.9	9.4	36.3	25.9	37.8	34.1	29.9			
Pr	1.52	1.48	1.68	1.2	1.61	1.57	1.38	1.34	4.91	3.51	5.02	4.56	3.89			
Nd	6.7	6.8	8.1	6.3	8.1	7.4	6.8	6.2	22.5	16.6	23.4	20.2	18.4			
Sm	1.51	1.53	2.13	1.19	1.83	1.7	1.77	1.62	5.39	3.97	5.91	4.81	4.9			
Eu	0.28	0.34	0.43	0.27	0.44	0.43	0.44	0.25	1.43	0.81	1.57	1.29	0.9			
Gd	2.09	1.95	2.29	1.85	2.53	2.1	2.26	1.91	6.15	4.61	6.51	5.3	4.84			
Tb	0.39	0.38	0.44	0.3	0.47	0.35	0.38	0.34	1	0.7	0.95	0.84	0.77			
Dy	2.86	2.95	3.54	2.55	3.72	2.93	3.16	2.86	7.51	5.12	7.28	5.92	5.92			
Ho	0.7	0.67	0.79	0.66	0.87	0.71	0.81	0.72	1.52	0.98	1.48	1.19	1.1			
Er	2.43	2.61	2.64	1.98	3.05	2.41	2.8	2.28	5.33	3.11	4.6	3.75	3.5			
Tm	0.31	0.36	0.38	0.3	0.42	0.35	0.41	0.35	0.72	0.42	0.65	0.5	0.52			
Yb	2.43	2.8	2.58	2.32	3.33	2.47	2.7	2.84	4.69	3.12	4.43	3.72	3.61			
Lu	0.34	0.41	0.37	0.33	0.51	0.38	0.39	0.39	0.74	0.45	0.64	0.53	0.5			
LREE	24.51	24.55	27.24	20.46	24.58	24.6	21.29	22.71	87.53	61.79	91	80.66	70.79			
HRRE	33.95	38.03	37.53	29.79	46.9	35.9	39.31	35.89	75.56	45.51	70.44	56.85	50.86			
ΣREE	64.89	68.65	70.24	56	75.85	65.08	64.97	64.59	176.14	116.03	174.44	149.61	136.1			
Element's ratios																
La/Sm	2.72	2.81	1.92	2.94	1.91	2.24	1.69	2.41	3.15	2.77	2.93	3.26	2.61			
Gd/Yb	0.86	0.70	0.89	0.80	0.76	0.85	0.84	0.67	1.31	1.48	1.47	1.42	1.34			

(Continued on the following page)

10.3389/feart.2024.1359617

TABLE 1 (*Continued*) Whole rock geochemical data from Wadi El-Mishama BIFs deposit (Central Eastern Desert, Egypt) for iron ore and wall rocks.

Facies	BIFs (Oxide Facies)								Metavolcanic rocks associated with the BIFs					Algoma-type	Superior-type	Rapitan-type
Sample Number	WM-1	WM-2	WM-3	WM-4	WM-5	WM-6	WM-7	WM-8	WM-9	WM-10	WM-11	WM-12	WM-13			
La/Yb	1.69	1.54	1.59	1.51	1.05	1.54	1.11	1.37	3.62	3.53	3.91	4.22	3.55			
Y/Ho	32.00	38.66	31.01	29.55	36.78	34.08	32.59	33.61	31.51	27.55	29.66	29.50	27.36			
Sm/Yb	0.62	0.55	0.83	0.51	0.55	0.69	0.66	0.57	1.15	1.27	1.33	1.29	1.36			
Sm/Lu	4.44	3.73	5.76	3.61	3.59	4.47	4.54	4.15	7.28	8.82	9.23	9.08	9.80			
Pr/Yb	0.63	0.53	0.65	0.52	0.48	0.64	0.51	0.47	1.05	1.13	1.13	1.23	1.08			
Eu/Sm	0.19	0.22	0.20	0.23	0.24	0.25	0.25	0.15	0.27	0.20	0.27	0.27	0.18			
U/Th	0.16	0.20	0.15	0.17	0.37	0.27	0.23	0.19	1.16	0.59	0.38	0.45	0.39			
Ni/Co	5.97	3.58	5.72	3.02	8.71	5.15	12.93	3.76	3.06	16.08	3.49	2.12	3.09			
Cu/Zn	0.59	0.31	0.78	0.24	1.37	1.18	0.80	0.40	0.66	0.36	0.26	0.26	0.66			
V/(V+Ni)	0.55	0.62	0.66	0.85	0.48	0.54	0.40	0.65	0.55	0.15	0.53	0.70	0.36			
PrN/YbN	0.197	0.166	0.205	0.163	0.152	0.200	0.161	0.148	0.329	0.354	0.357	0.386	0.339			
La/La ∗	1.15	1.53	1.80	8.57	2.53	1.50	1.97	1.60	1.80	1.99	1.98	1.50	2.09			
Ce/Ce ∗	0.93	0.90	0.91	0.88	0.83	0.88	0.84	0.93	0.91	0.95	0.93	0.92	0.97			
Pr/Pr ∗	1.01	0.98	0.97	0.91	0.99	1.00	1.00	0.97	0.95	0.94	0.94	0.97	0.92			
Eu/Eu ∗	0.73	0.89	0.88	0.91	0.95	1.11	1.07	0.67	1.21	0.95	1.28	1.25	0.89			

Note: BIFs, Banded Iron Formations; LOI, Loss on Ignition; Fe2O3T, All Fe calculated as Fe2O3; REE, Rere Earth Element; PAAS, Post Archean Australian Shale, subscript N= PAAS normalizing factors after Taylor and McLennan (1995). La/La* ={La PAAS/(3 × Pr PAAS -2 × Ho PAAS)}; Ce/Ce* = {Ce PAAS/(La PAAS × Pr PAAS)1/2}; Pr/Pr* = Pr PAAS/(Ce PAAS × Nd PAAS)1/2; Eu/Eu* = Eu PAAS/(Sm PAAS × Gd PAAS)1/2} (after Bolhar et al., 2004); The less-than sign (<) indicates that the value is below detection limit. ΣREE= Sum of Rere Earth Elements. Algoma-type and Superior-type after Gross and McLeod (1980); Rapitan-type BIFs after Klein and Beukes (1993). Blank space= not detected.

10.3389/feart.2024.1359617

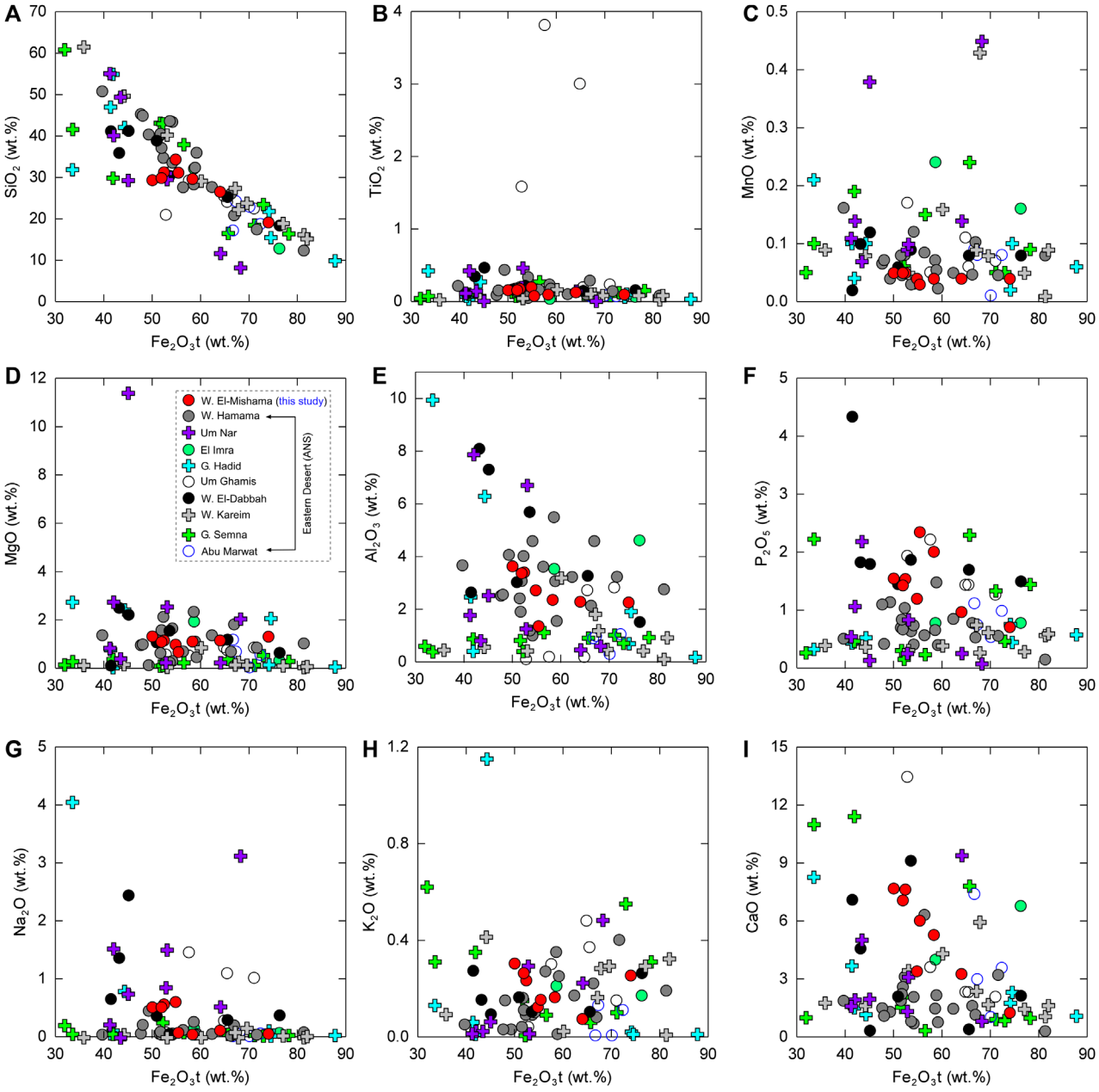

FIGURE 5
(A–I) Covariant relationship between $Fe_2O_3^t$ vs. major elements. Data of Arabian–Nubian Shield from Abd El-Rahman et al. (2019); El-Shazly et al. (2019).

4.1.2 Metavolcanic rocks

The analytical results of the studied volcanic rocks are presented in Table 1. The bulk chemical compositions of hosting units for Algoma-type BIFs from the literature (i.e., Eastern Desert; Khalil et al., 2015; El-Shazly et al., 2019) are also used to discuss the possible source of parent magma and the formation setting of wall units (Supplementary Table S2).

4.2 Pb isotopic composition

Lead isotopic compositions for seven iron ore samples from the Wadi El-Mishama deposit are presented in Supplementary Table S3. $^{206}Pb/^{204}Pb$ values range from 16.67 to 19.80 with an average of 17.71. $^{207}Pb/^{204}Pb$ values are between 14.33 and 16.00 with an average of 15.38; whereas $^{208}Pb/^{204}Pb$ values are from 34.67 to 39.20 with an average of 37.27.

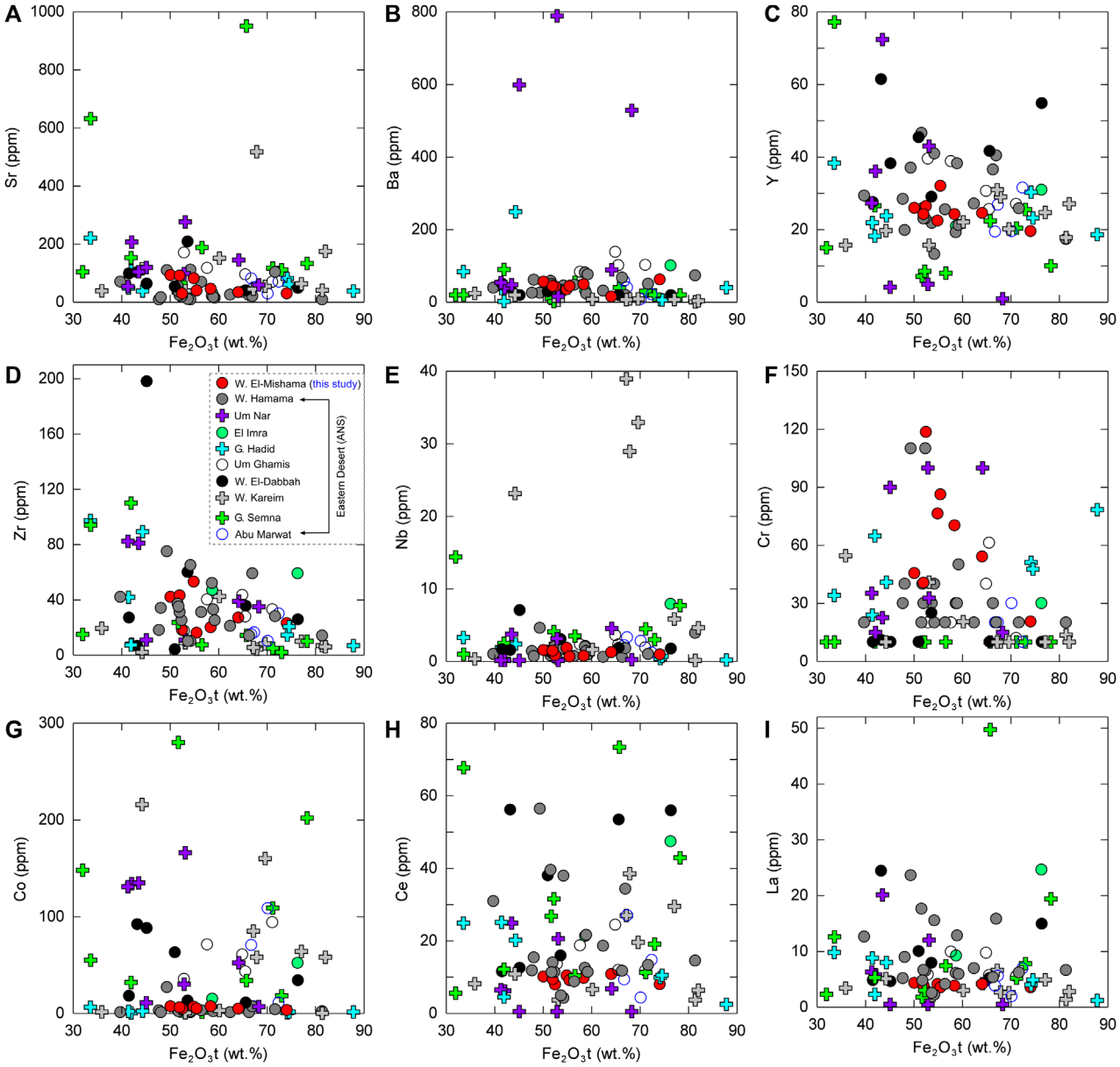

FIGURE 6
(A–I) Variation diagrams of $Fe_2O_3^t$ vs. trace elements. Data of Arabian–Nubian Shield from (Abd El-Rahman et al., 2019); El-Shazly et al. (2019).

5 Discussion

5.1 Depositional environment

The depositional environment of BIFs has been a subject of considerable debate. Regionally, it has been proposed that the most likely tectonic environments from which iron may have been released and then accumulated as BIFs are mid-oceanic ridges or hot spots (Dalstra et al., 2008). Algoma-type BIFs are most commonly found in Precambrian successions that contain a significant proportion of submarine volcanic rocks. These stratigraphic horizons were formed in oceanic arc and back-arc environments (Peter, 2003). More especially, numerous giant and world-class BIFs were created during intra-plate tectonic-thermal and rifting episodes (Pirajno and Bagas, 2008). It is well known that the Precambrian Algoma-type BIFs are stratigraphically and genetically linked to VMS mineralization in many cases worldwide (e.g., Qingyuan greenstone belt, North China and Abitibi greenstone belt, Canada) (Taner and Chemam, 2015; Peng et al., 2022). The precipitation of iron ores may be found close to or distal from the high-temperature up-flow zone of VMS-related submarine magmatic-hydrothermal activity (Peter et al., 2014). Locally, the iron successions in the Egyptian Eastern Desert have been linked to volcanic eruptions and

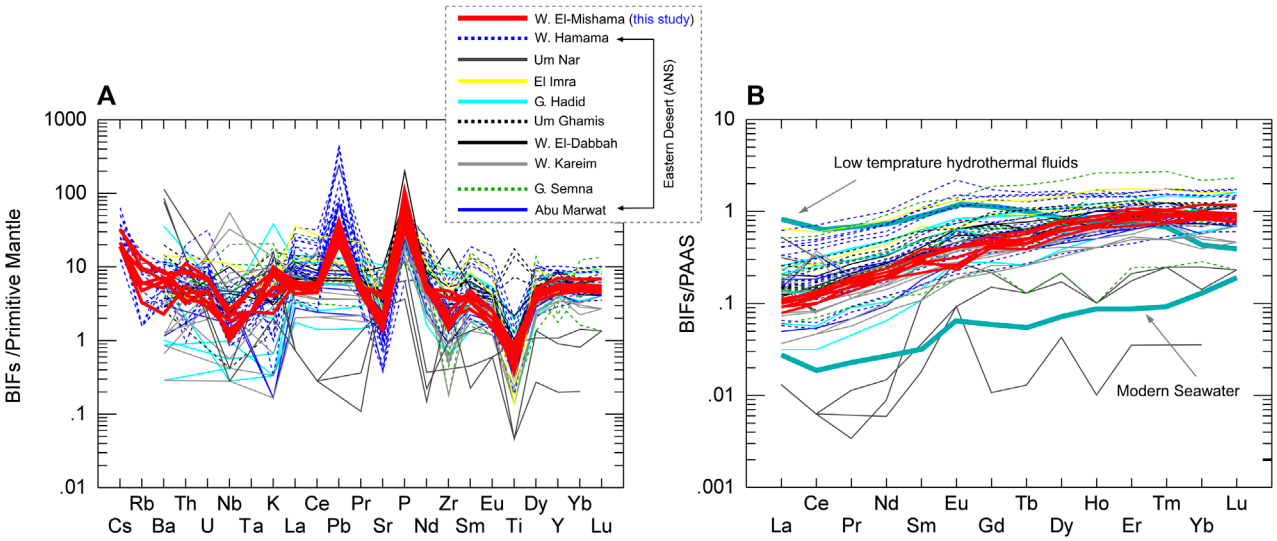

FIGURE 7
(A) Primitive mantle-normalized spider diagram for Wadi El-Mishama BIFs and some BIFs from Arabian–Nubian Shield. Normalizing values are from Sun and McDonough (1989); **(B)** Post Archean Average Shale (PAAS)-normalized REE for Wadi El-Mishama BIFs and some BIFs from Arabian–Nubian Shield. Normalizing values are from Taylor and McLennan (1985). Data of Arabian–Nubian Shield (ANS) from (Abd El-Rahman et al., 2019); El-Shazly et al. (2019).

are proposed to originate in an intra-back-arc basin setting (Faisal et al., 2022).

Based on the Nb/Y versus Zr/Ti classification diagram (Figure 8A) (Winchester and Floyd, 1977), the studied host rocks showed variance between andesitic to rhyolitic compositions. They have a transitional affinity (tholeiitic - calc-alkaline) on the Zr/Y vs. Th/Yb diagram (Figure 8B). The tectonic discrimination diagrams show clearly that these rocks mainly plot within island arc setting fields, indicating the oceanic nature of the BIF host rocks (Figures 8C, D). The high field strength elements (HFSEs, e.g., Zr, Hf, Nb, Ta, P, and Ti) and HREE values are helpful markers for determining potential tectonic settings of extrusive rocks (Pearce, 2008). In the Ti against Zr tectonic discrimination diagram (Figure 8C), the host rocks of Wadi El-Mishama BIFs lie mainly in the island arc field. According to the Th/Yb versus Nb/Yb diagram (Figure 8D), the studied units have an affinity to oceanic island arcs. This suggests that the iron sequence of the Wadi El-Mishama area is typical of an intra-oceanic arc setting (i.e., back-arc basin). This result is in agreement with the depositional environment of island arcs from the Egyptian Eastern Desert which, were deposited in a back-arc spreading tectonic setting during the closure of the Mozambique Ocean (Faisal et al., 2020).

5.2 Source characteristic and depositional process

5.2.1 Detrital input

Iron formations are typically detritus-free, however, terrigenous contamination has been documented throughout the world (Hou et al., 2019). In general, some oxides (Al_2O_3 and TiO_2), transition metals, HFSEs, and LILE are suitable monitors for detecting terrigenous contamination. During hydrothermal, diagenetic, and weathering processes, aluminum and titanium are thought to be largely immobile (MacLean and Kranidiotis, 1987). The studied BIFs exhibit relatively low Al_2O_3 + TiO_2 contents ranging from 1.46 to 3.81 wt.% (Table 1), with a positive correlation between them (Figure 9A) suggesting the presence of terrigenous components during their deposition (Barrote et al., 2017). In addition, a clastic component of igneous origin may have been present in the examined samples due to relatively high Cr (20.5–118.5 ppm, Table 1) and Zr (16–53 ppm) values (Bolhar et al., 2004).

The Y/Ho (29.55–38.66) values of the studied BIFs, display little admixture of clastic and volcanic components during their deposition (Bolhar et al., 2004). The BIF samples have Eu anomalies of 0.88–1.11 (Figure 7B), consistent with low terrigenous input. Relatively higher values of Sr and Y (Table 1) indicate the presence of a source of crustal felsic rocks (i.e., these components are generally produced from the weathering of crustal felsic rocks) (Rao and Naqvi, 1995). Thus, all these features suggest that the Wadi El-Mishama iron deposit was variably influenced by detrital materials. The studied BIFs samples plot close to the East Pacific Rise hydrothermal metalliferous sediments field in the Fe/Ti versus Al/(Al+Fe+Mn) diagram (Figure 9B), which suggests that they are characterized by a low proportion (less than 20%) of detrital components. It is consistent with low U/Th values (i.e., Wadi El-Mishama BIFs vary from 0.15 to 0.37) that are typical of relatively pure chemical iron formations (Thurston et al., 2012).

5.2.2 Hydrothermal activity

The immobile elements play a key role in understanding metallogenetic evolution, and the REEs signature of iron deposits has been employed as a proxy to determine the origin of silica and iron (Soh Tamehe et al., 2018). The LREE depletion, HREE enrichment, and positive La anomalies of the studied

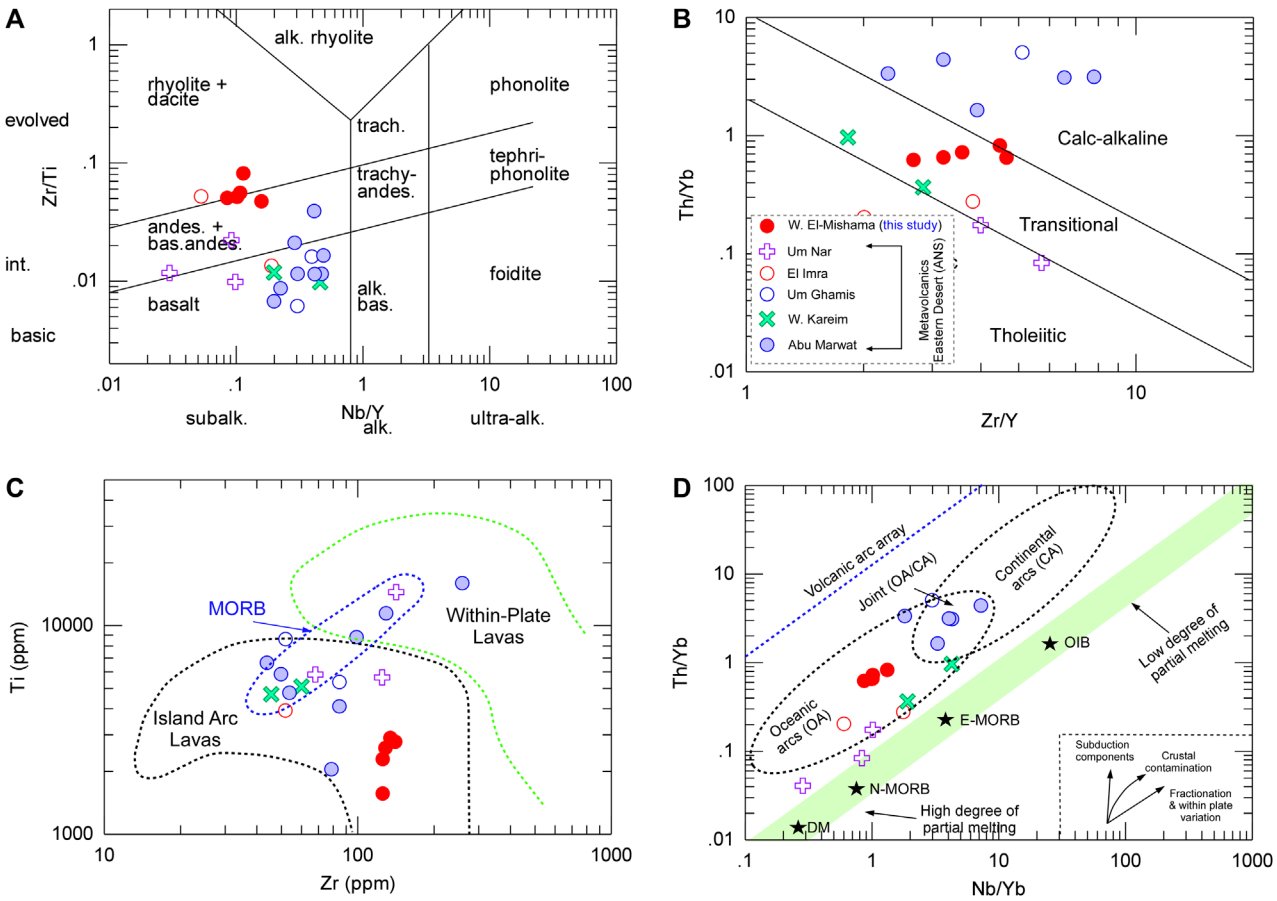

FIGURE 8
Classification diagrams of studied metavolcanics host rocks: **(A)** Zr/Ti vs. Nb/Y diagram (Winchester and Floyd, 1977); **(B)** Zr/Y vs. Th/Yb diagram (Ross and Bédard, 2009); Tectono-magmatic discrimination diagrams of studied metavolcanics host rocks for Wadi El-Mishama BIFs and some BIFs from Arabian–Nubian Shield: **(C)** Ti against Zr tectonic discrimination diagram (Pearce, 1982); **(D)** Th/Yb versus Nb/Yb diagram (Pearce, 2014). Abbreviation: DM= Depleted Mantle, OIB= Ocean Island Basalt, VAT= Volcanic Arc Tholeiites, OFB= Oceanic Flood Basalts, FAB= Fore-Arc Basalt, E-MORB: Enriched Mid-Ocean Ridge Basalt; N-MORB: Normal Mid-Ocean Ridge Basalt. Data of Arabian–Nubian Shield from (Khalil et al., 2015); El-Shazly et al. (2019).

BIFs indicate seawater signatures to some extent (Bolhar et al., 2004; Soh Tamehe et al., 2018). U enrichment, which is normally enriched in the evolved crust, is usually reflected a detrital contribution to BIFs deposits (Taylor and McLennan, 1985; Sylvestre et al., 2017). In contrast, U depletion is mostly linked to oxic, early-diagenetic alteration resulting in the release of U back into seawater (Dunk and Mills, 2006). The BIFs samples contain relatively lower concentrations of U (0.06–0.15 ppm) compared to Th (0.27–0.94 ppm), which is indicative of their exposure to seawater with a slow rate of accumulation (Roy and Venkatesh, 2009). On the REE patterns normalized PAAS plot (Figure 7B), the samples lie between the average composition of low-temperature hydrothermal solutions and South Pacific seawater. The Zr/Hf against Y/Ho plot (Figure 10A) signifies that most of the data are super-chondritic (Y/Ho > 27.7), pointing to the interaction of hydrothermal fluids with seawater as well as certain potential sources of hydrogenous-detrital contamination (i.e., volcanic input or terrigenous clastic materials from country rocks). The ratios of Eu/Sm and Sm/Yb reflect the rates of reaction between hydrothermal fluids (0.1%–5%) and seawater during the deposition of BIFs (Figure 10B; Alexander et al., 2008), that is, a 1000:1 to 100:5 mixture of seawater and high-temperature hydrothermal fluids. The ratio of seawater to hydrothermal fluids is further emphasized by using the discrimination diagrams of Alexander et al. (2008) (e.g., Sm/Yb vs. Eu/Sm; Figure 10B), where samples accumulate close to seawater and low-temperature hydrothermal fluids (<0.1%) fields and far away from high-temperature hydrothermal fluids.

The obvious positive Eu anomalies in Archean and Paleoproterozoic BIFs suggest that sub-oceanic waters were affected by hydrothermal fluids from deep-sea spreading sites (e.g., Bau and Dulski, 1996; Bolhar et al., 2004; Planavsky et al., 2010). More specifically, high-temperature hydrothermal fluids (>250°C) are characterized by strong positive Eu anomalies, whereas low-temperature fluids (<200°C) are characterized by weak to no positive Eu anomalies (Basta et al., 2011). Variations in the hydrothermal fluid ratios to seawater, as well as the mobilization of Eu at temperatures above 200°C during the alteration or metamorphism of the ores, could have caused changes in the intensity of the Eu anomalies (Bolhar et al., 2004). So, the weak positive Eu anomalies

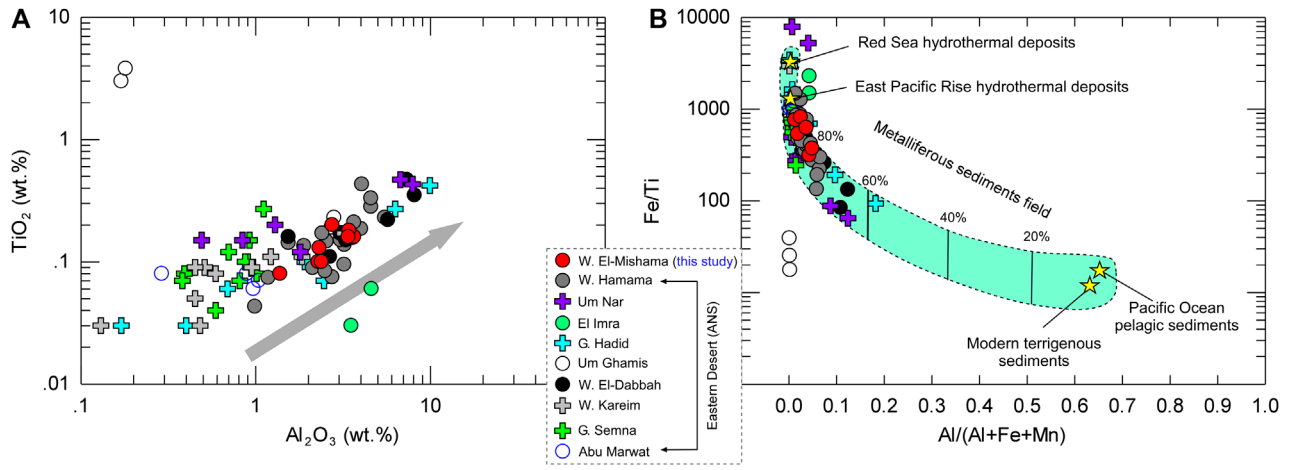

FIGURE 9
(A) Al_2O_3 vs. TiO_2 diagram; **(B)** Relationship between Fe/Ti vs. Al/(Fe + Mn + Al) (Boström, 1973; Peter et al., 2003), estimating the relative contribution from the hydrothermal input. The curve represents the mixing of East Pacific Rise deposits (EPR) with pelagic sediments (PC) whereas the numbers indicate the approximate percentage of EPR in the mixture (adopted from Barrett (1981). Also indicated are compositions for the mean upper continental crust (UC) (Taylor and McLennan, 1985), Red Sea hydrothermal deposits (RS) (Marchig et al., 1982), and the Cyprus Umber (CU) (Robertson and Hudson, 1973). The light green zone represents ideal mixing between "metalliferous and terrigenous sediment" and between "metalliferous and Pacific Ocean pelagic sediment." Data of Arabian–Nubian Shield from (Abd El-Rahman et al., 2019); El-Shazly et al. (2019).

of the studied BIFs are consistent with low-temperature (<250°C) shallow hydrothermal volcanic exhalative systems.

The high Y/Ho values in some fluids can result from the mixing of seawater and hydrothermal fluids during REE scavenging by iron (oxy) hydroxide minerals. As mentioned previously, the Y/Ho values in the studied BIFs are super-chondritic (Y/Ho > 27.7), and similar to those of most Neoproterozoic BIFs (mean Y/Ho = 29.2; n = 77) (Cox et al., 2013). Additionally, this does not imply that a high-temperature hydrothermal input occurred. The iron samples from the study area have low Cu (3.27–16.05 ppm) and Zn (7.8–25 ppm) concentrations that are relatively near to the crustal background levels of these metals (Angerer et al., 2012), indicating the studied BIFs deposit was likely formed from low-temperature (<250°C) hydrothermal fluids without significant accumulation of Cu-Zn massive sulfide or were formed distal from the high-temperature up-flow zone of VMS-related magmatic-hydrothermal system.

The Fe/Ti versus Al/(Al + Fe + Mn) diagram reveals the ratios of hydrothermal fluids to the detrital contamination of clastic inputs during BIF deposition. All collected samples plot close to the field of East Pacific Rise hydrothermal sediments (Figure 9B). Due to the low Al_2O_3 content (1.38–3.65) of the examined iron ores, hydrothermal solutions rather than detrital mineral assemblages were responsible for the weak positive Eu_{PAAS} anomalies. Also, these Eu_{PAAS} anomalies signify that the fluids that carried SiO_2 and FeO to the ambient ocean were derived from a reducing environment (Campbell et al., 1988). Furthermore, the hosting volcanic lavas display positive Eu anomalies (Table 1).

In the Co/Zn versus $Fe_2O_3{}^T$ diagram (Figure 10C), all samples were plotted on the hydrothermal field (Toth, 1980). Klein and Beukes (1989) developed the relationship between ΣREE and Σ (Co + Cu + Ni) of hydrogenous and hydrothermal deposits to construct the fields of these deposits (Figure 10D). According to this diagram, the majority of the studied BIFs are located close to the area where hydrothermal deposits are present. This suggests that a significant portion of the iron in the investigated BIFs was added to the seawater by hydrothermal solutions derived from hydrothermally active marine environments. All BIF samples are shown to plot on the field of hydrothermal origin in the Fe–Al–Mn triangular discrimination diagram (Figure 11A). Therefore, we propose that the Wadi El-Mishama iron deposit was precipitated from a mixture of seawater and low-temperature hydrothermal fluids (<200°C) with variable detrital contamination.

5.2.3 Redox conditions

It has been suggested that the ancient oceans at the beginning of the Neoproterozoic Era were dominantly in an anoxic state (Tostevin et al., 2016). The Ni/Co and V/(V + Ni) values are commonly used to evaluate the paleo-redox conditions (Jones and Manning, 1994). It has been shown that Ni/Co values of <5 indicate oxic conditions, whereas the values of >5 exhibit dysoxic states (i.e., very low oxygen concentration, between anoxic and hypoxic) in the deposition area (Jones and Manning, 1994). Ni/Co values of the analyzed iron samples display dysoxic conditions (avg.= 6.11). On the other hand, V/(V + Ni) values from 0.50 to 0.60 suggest oxic conditions, whereas values from 0.60 to 0.85 represent anoxic conditions (Rimmer, 2004). In the present study, V/(V + Ni) values have an average of 0.59, which is at the interface between oxic and anoxic conditions. Ce responds to changes in the redox state. Compared to shale composites, oxic water has a negative Ce anomaly, whereas the underlying anoxic water lacks this negative anomaly and may exhibit a small positive Ce anomaly (de Baar et al., 1988). The collected ores display weak negative or no Ce_{PAAS} anomalies, implying suboxic to oxic conditions. A lack of a noticeable Ce anomaly in hydrothermal iron-rich crusts (modern basins) was attributed by Stoffers et al. (1993) to the mixing of hydrothermal fluids with seawater. Furthermore, Ce/Ce ∗ values

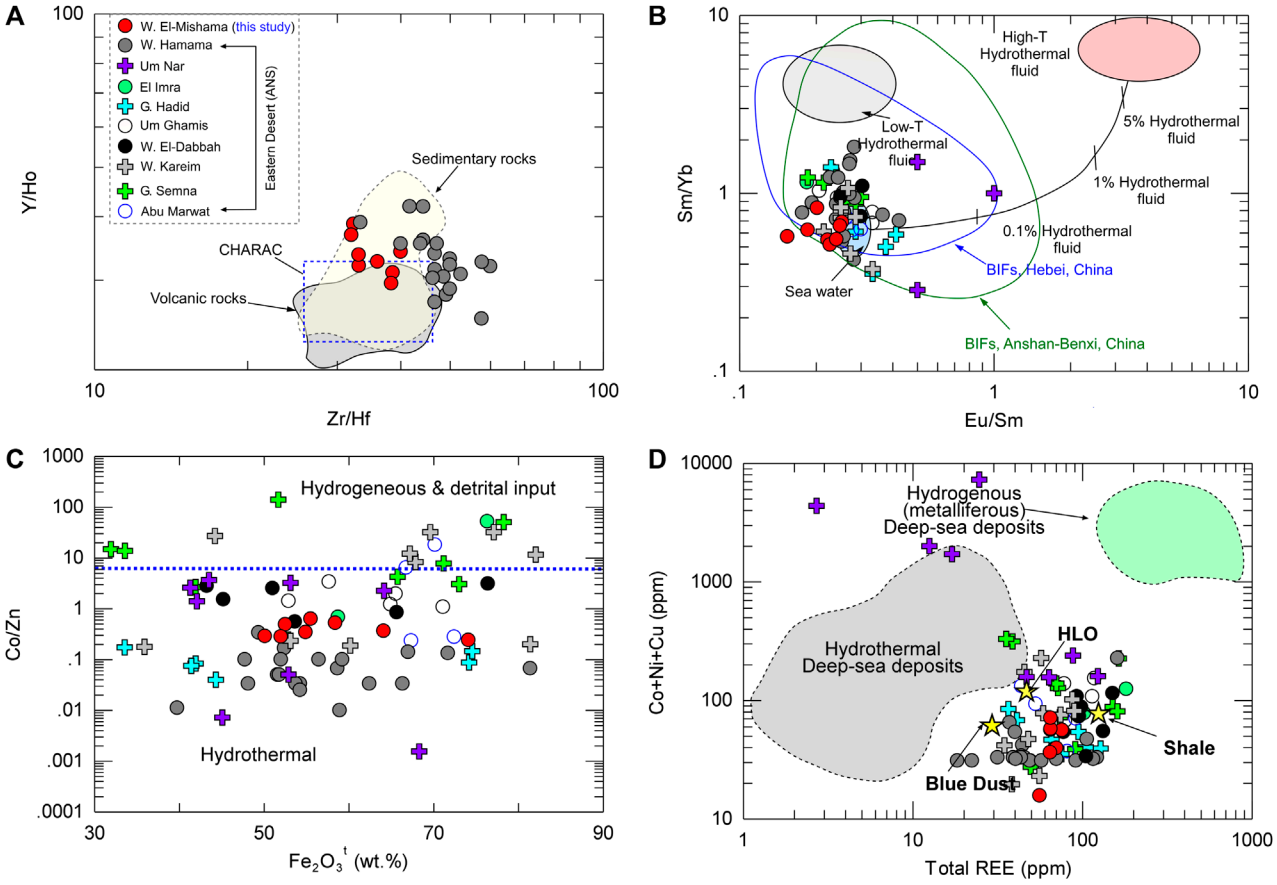

FIGURE 10
(A) Y/Ho vs. Zr/Hf ratios for studied BIFs with typical fields of CHARAC (CHarge and Radius Controlled), volcanic and clastic sedimentary rocks (Bau and Dulski, 1999), **(B)** Y/Ho vs. Sm/Yb elemental ratio plots: two-component conservative mixing model (modified from Alexander et al., 2008) for the studied BIFs. The average composition of high-temperature (>350°C) hydrothermal fluids based on Bau and Dulski (1999), low-T hydrothermal solutions from Marchig et al. (1982), and Pacific seawater based on Alibo and Nozaki (1999); **(C)** Co/Zn vs. Fe_2O_3 discrimination diagram for studied BIFs, separating exhalative hydrothermal BIFs from the hydrogenous-detrital input (Toth, 1980). The approximate Co/Zn ratio in the dotted line is after Toth (1980); **(D)** ΣREE vs. Co + Ni + Cu [modified after Dymek and Klein (1988)]; Data of Arabian–Nubian Shield from Abd El-Rahman et al. (2019), El-Shazly et al. (2019).

below ~0.10 suggest oxic conditions, whereas the ratios above 0.10 reflect anoxic conditions (Wright et al., 1987). The data from the study area have Ce/Ce∗ ranging from 0.83 to 0.93 which clearly shows anoxic events during the formation of iron deposits. Moreover, it has been proposed that a negative Ce anomaly can be divided into three groups: (a) ~0.9–1.0; (b) ~0.6–0.9; and (c) <0.5 which represents anoxic, suboxic, and oxic marine water, respectively (Chen et al., 2015). The studied BIF samples plot mainly on the positive La anomaly field (with no distinguished Ce anomaly) in the $(Pr/Pr*)_{PAAS}$ vs. $(Ce/Ce*)_{PAAS}$ diagram (Figure 11B) and completely in the field of late Paleoproterozoic BIFs deposits, which reflect a suboxic to anoxic condition during BIF precipitation (Wang et al., 2016). Conclusively, the Ce/Ce∗ values documented by the investigated BIFs reflect that the sediments were mainly deposited at the transition between suboxic and anoxic conditions. The U/Th values of >1.25 signify anoxic conditions (Nath et al., 1997). The U/Th values of the studied BIFs vary from 0.15 to 0.37, which are consistent with suboxic to oxic conditions. In addition, on the PAAS-normalized diagram, oxic water is commonly characterized by HREE enrichment compared with anoxic water (German et al., 1991). LREE are more susceptible to removal from solution through adsorption reactions, while HREE are almost entirely bound by stable carbonate complexes (Byrne and Kim, 1990; Byrne and Sholkovitz, 1996; Alibo and Nozaki, 1999). For example, cerium displays a strong negative anomaly On the PAAS-normalized REE pattern for an oxygenated marine environment (Ce^{III} oxidized to Ce^{IV}), while no noticeable negative anomaly in a suboxic and anoxic environment (Byrne and Sholkovitz, 1996; Ohta and Kawabe, 2001). LREE-depletion relative to HREE in the PAAS-normalized diagram of the studied BIFs samples (Figure 7B) suggests the deposition has occurred under slightly oxidized seawater. Furthermore, several metals are commonly to be complexed by natural organic substances, for example, zinc is largely complexed in the upper water column than copper (Bruland, 1989; Donat and Bruland, 1990). Thus, low Cu/Zn values largely signify oxidizing environments in the depositional basin, whereas high Cu/Zn values imply reducing conditions (Hallberg, 1976; Nagarajan et al., 2007; Ngueutchoua et al., 2017). The Cu/Zn values

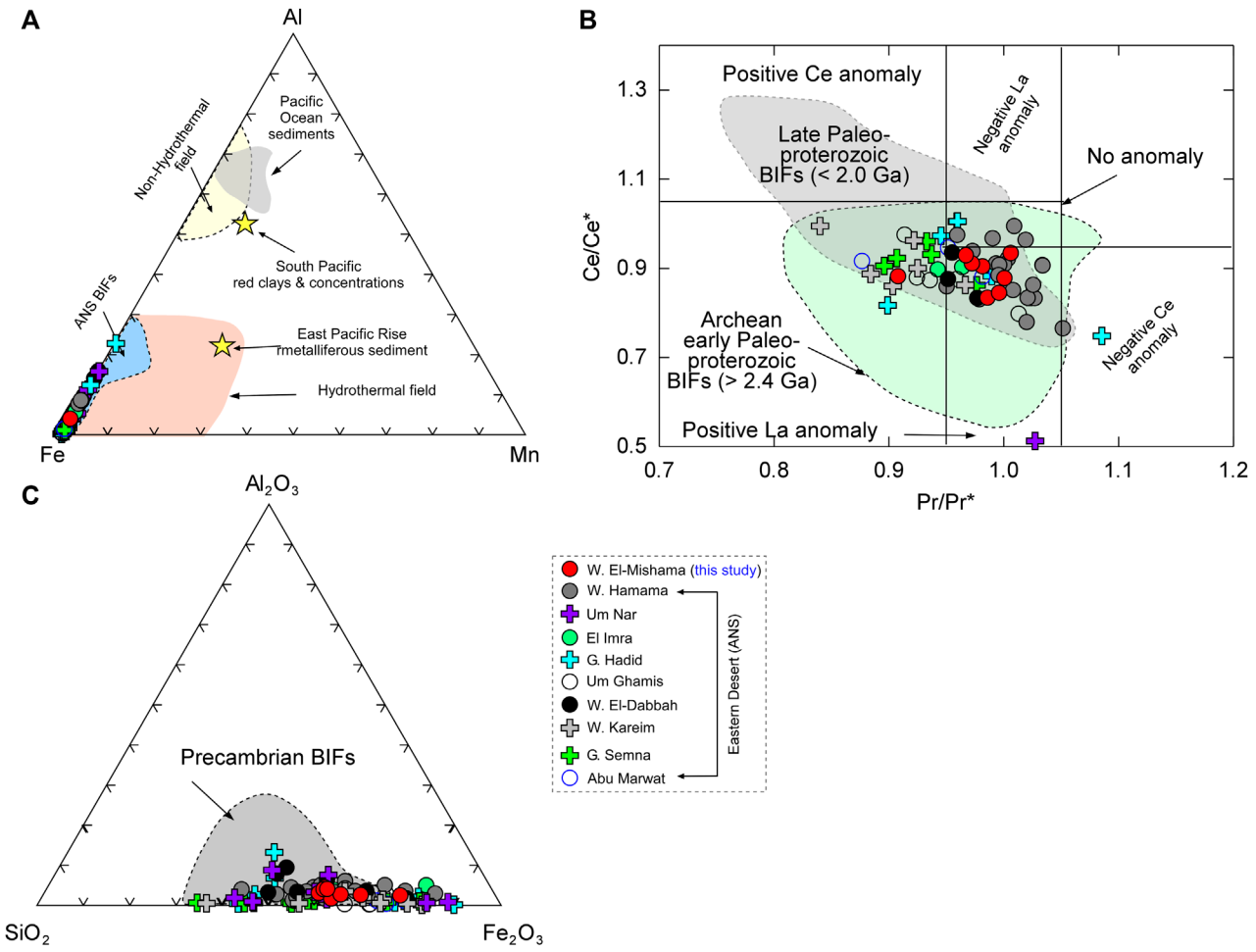

FIGURE 11
(A) Fe–Mn–Al (wt%) ternary diagram discriminating between hydrothermal and nonhydrothermal end members for modern marine ferromanganese deposits (Boström, 1973). ANS BIFs plot within the hydrothermal field. The fields for metalliferous sediments from the East Pacific Rise and other oceanic sediments are also shown (Boström, 1973); **(B)** PAAS normalized Ce/Ce ∗ and Pr/Pr ∗ used to distinguish between La and Ce anomaly in studied BIFs(Bau and Dulski, 1996). Field of late Paleoproterozoic BIFs (<2.0 Ga) after Planavsky et al. (2010); field of Archean and early Paleoproterozoic BIFs (>2.4 Ga) after Planavsky et al. (2010); Zhang et al. (2011); Dai et al. (2012). **(C)** SiO_2–Al_2O_3–$Fe_2O_3^T$ discrimination diagram of studied BIFs plotted within the Precambrian field (Govett, 1966). Data of Arabian–Nubian Shield from (Abd El-Rahman et al., 2019); El-Shazly et al. (2019).

of the studied ores range from 0.24 to 1.37, which are suggestive of oxic conditions. Consequently, the above-mentioned geochemical signatures indicate that the sedimentary environment of the Wadi El-Mishama BIFs was primarily dysoxic to oxic.

5.3 Comparison with other Algoma-type BIFs

A comparative study of the major and trace element contents of Wadi El-Mishama BIFs with BIFs from other regions within the ANS (Figures 5, 6; Supplementary Table S2) shows that there is a significant degree of consistency and similarity. The SiO_2–Al_2O_3–$Fe_2O_3^T$ (Figure 11C) (Govett, 1966) ternary diagrams show that the studied iron ores plot closer to the Fe_2O_3 apex and within the field of Algoma-type Precambrian BIFs, thus implying a closer chemical similarity to other Precambrian iron deposits. Some iron samples from BIFs of the Gebel Semna, Um Ghamis, and Wadi Kareim areas are variable in their REE patterns due to weathering and metamorphism effects. No notable positive Eu anomalies were found in the examined iron ores (Eu/Eu_{PAAS} = 0.88–1.11; Figure 7B), which is consistent with other Neoproterozoic iron deposits. It is noteworthy that Algoma-type iron deposits typically exhibit a weak negative Ce anomaly that resembles seawater (Aftabi et al., 2021). The investigated iron formations primarily exhibit negligible to small negative Ce anomalies (Ce/Ce_{PAAS} = 0.83–0.93) that are similar to those recorded in the ANS iron deposits (Figure 7B).

Genetically, two hypotheses have been proposed for the formation of ANS BIF deposits. The first view is that they have been linked to global glaciations (Snowball Earth episodes) similar to Rapitan-type BIF. More specifically, Stern et al. (2006) and Ali et al. (2010) attributed the formation of iron deposits at Wadi Kareim, Central Eastern Desert (Figure 1, location no. 6) to the Sturtian glaciation event with evidence of glacial diamictite deposited with iron ores. The lack of glacial/ice-transported detritus

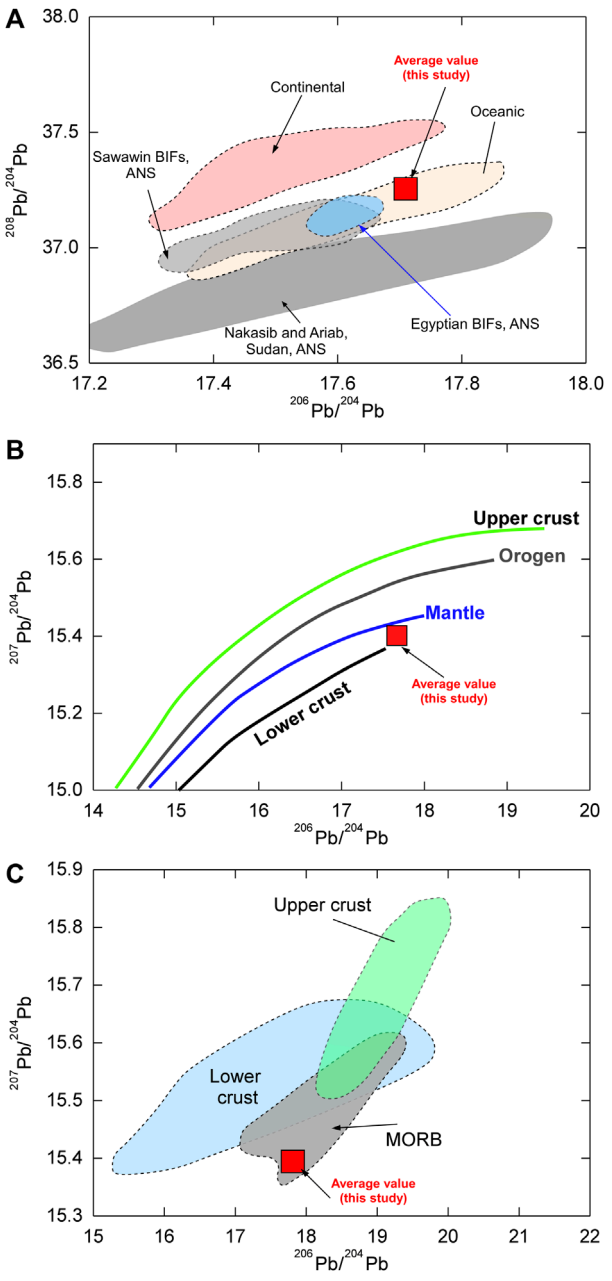

FIGURE 12
Lead isotope diagrams of iron ore for the Wadi El-Mishama deposit. **(A)** Plot of $^{208}Pb/^{204}Pb$ vs. $^{206}Pb/^{204}Pb$; **(B,C)** Plots of $^{207}Pb/^{204}Pb$ vs. $^{206}Pb/^{204}Pb$. The field for Sawawin BIFs (Saudi Arabia) and Egyptian BIFs is taken from Stern et al. (2013). The field of Nakasib and Ariab, NE Sudan is taken from Stern and Abdelsalam (1998) for feldspar data. Continental and oceanic fields are taken from Stacey et al. (1980) for galena data from the Saudi Arabian Shield. Evolution curves of the upper crust, orogen, mantle, and lower crust in Figure **(B)** are taken from Zartman and Doe (1981). The fields of major terrestrial reservoirs in Figure **(C)** are taken from White (2013).

(sedimentological evidence of glaciation) in the study area suggests that the Snowball Earth hypothesis is not fully convincing for the investigated iron formations. The other model is that they were formed in a tectonically and magmatically active basin during the closure of the Mozambique Ocean (Abd El-Rahman et al., 2019; El-Shazly et al., 2019; Kiyokawa et al., 2020). The extensive association of the volcanic and volcaniclastic rocks with the iron formations is a common observation in this model.

The Wadi El-Mishama BIFs are intimately associated with volcanic units that formed within an intra-oceanic arc setting based on the resultant tectonic discrimination diagrams (Figures 8C, D). As a result, the iron was most likely sourced from hydrothermal vent fluids. Moreover, these features are largely in agreement with those proposed in previous studies in the Egyptian Eastern Desert (Abd El-Rahman et al., 2019; El-Shazly et al., 2019). This conclusion is also supported by relatively homogeneous, low radiogenic Pb isotopic ratios from the study area which plotted close to the field of BIFs from the ANS and within the oceanic field on the $^{206}Pb/^{204}Pb$ versus $^{208}Pb/^{204}Pb$ binary diagram (Figure 12A). This is a sign that the Pb metal was derived from geological bodies that had homogeneous Pb isotopes or those that had varied Pb isotopes but were homogenized prior to precipitation within extensional geodynamic regimes (i.e., an intra-oceanic arc environment) over a relatively restricted period. Besides, the current isotopic data lies in the area between the mantle and the crust (Figure 12B) and overlaps that of the Pb isotopic composition of MORB (Figure 12C). It demonstrates that Pb metal may have originated from the same source of iron and base metals (i.e., magmatic-hydrothermal fluids and leaching of basement lithologies).

Based on the above discussion, we suggest that Wadi El-Mishama BIFs have geochemical signatures of modern iron-rich crusts that their formation is connected to low-temperature shallow hydrothermal volcanic exhalative systems related to suboxic to oxic basins. Lastly, the Wadi El-Mishama and other BIFs from the ANS have quite similar geochemical fingerprints, which could point to a similar mechanism of formation from hydrothermal vent fluids.

6 Concluding remarks

Based on the above-mentioned analyses and discussion, the main findings of this research can be summarized as follows:

(1) The Wadi El-Mishama area (Central Eastern Desert, Egypt) is an Algoma-type BIFs prospect that is hosted in Neoproterozoic Island arc assemblages. Their precipitations incorporated a low proportion of detrital components at low-temperature (<200°C) hydrothermal solutions mixed with seawater. Moreover, the iron deposition occurred in a submarine environment under mildly oxidized conditions.

(2) A back-arc basin seems to be the most likely extensional tectonic regime for the accumulation of Wadi El-Mishama BIFs. The field relationship, petrography, geochemistry, tectonic setting, and mechanism of formation of the studied iron ores are fully compatible with that of Neoproterozoic BIFs from the ANS.

(3) It is recommended that future research should focus on advanced geochemical and stable isotope investigations to develop a better genetic model, as well as geochronology studies that help in determining the duration of igneous activities that had been occurring in the region.

Data availability statement

The datasets presented in this study can be found in online repositories. The names of the repository/repositories and accession number(s) can be found in the article/Supplementary Material.

Author contributions

MS: Data curation, Investigation, Resources, Supervision, Writing–original draft, Writing–review and editing. MF: Data curation, Investigation, Software, Visualization, Writing–original draft, Writing–review and editing. ML: Data curation, Formal Analysis, Funding acquisition, Methodology, Visualization, Writing–original draft. IS: Data curation, Funding acquisition, Investigation, Methodology, Project administration, Software, Validation, Visualization, Writing–review and editing. MA: Writing–review and editing, Data curation, Investigation, Funding acquisition, Software. EL: Conceptualization, Formal Analysis, Investigation, Methodology, Resources, Software, Validation, Writing–original draft.

Funding

The author(s) declare that financial support was received for the research, authorship, and/or publication of this article. This research was funded by the Canada First Research Excellence Fund, through the Arthur B. McDonald Canadian Astroparticle Physics Research Institute. This research was also funded by Researchers Supporting Project Number (RSP2024R455), King Saud University, Riyadh, Saudi Arabia. This funding has been instrumental in the progression and success of our research.

Acknowledgments

We appreciate useful comments and advice from two reviewers and editorial handling by Paola Marianelli which improved the text and data interpretation. The authors are indebted to Hassan Osman for field assistance and photomicrographs. We gratefully acknowledge the financial support for this work provided by the Canada First Research Excellence Fund through the Arthur B. McDonald Canadian Astroparticle Physics Research Institute. This funding has been instrumental in the progression and success of our research. This research was also funded by Researchers Supporting Project Number (RSP2024R455), King Saud University, Riyadh, Saudi Arabia.

Conflict of interest

The authors declare that the research was conducted in the absence of any commercial or financial relationships that could be construed as a potential conflict of interest.

Publisher's note

All claims expressed in this article are solely those of the authors and do not necessarily represent those of their affiliated organizations, or those of the publisher, the editors and the reviewers. Any product that may be evaluated in this article, or claim that may be made by its manufacturer, is not guaranteed or endorsed by the publisher.

Supplementary material

The Supplementary Material for this article can be found online at: https://www.frontiersin.org/articles/10.3389/feart.2024.1359617/full#supplementary-material

References

Abdelfadil, K. M., Saleh, G. M., Putiš, M., and Sami, M. (2022). Mantle source characteristics of the late Neoproterozoic post-collisional gabbroic intrusion of Wadi Abu Hadieda, north Arabian-Nubian Shield, Egypt. *J. Afr. Earth Sci.* 194, 104607. doi:10.1016/j.jafrearsci.2022.104607

Abd El Monsef, M., Sami, M., Toksoy-Köksal, F., Abart, R., Ondrejka, M., and Abdelfadil, K. M. (2023). Role of magmatism and related-exsolved fluids during Ta-Nb-Sn concentration in the central Eastern Desert of Egypt: evidences from mineral chemistry and fluid inclusions. *J. Earth Sci.* 34, 674–689. doi:10.1007/s12583-022-1778-y

Abd El-Rahman, Y., Gutzmer, J., Li, X.-H., Seifert, T., Li, C.-F., Ling, X.-X., et al. (2019). Not all Neoproterozoic iron formations are glaciogenic: Sturtian-aged non-Rapitan exhalative iron formations from the Arabian–Nubian Shield. *Miner. Deposita* 55, 577–596. doi:10.1007/s00126-019-00898-0

Aftabi, A., Atapour, H., Mohseni, S., and Babaki, A. (2021). Geochemical discrimination among different types of banded iron formations (BIFs): a comparative review. *Ore Geol. Rev.* 136, 104244. doi:10.1016/j.oregeorev.2021.104244

Alexander, B. W., Bau, M., Andersson, P., and Dulski, P. (2008). Continentally-derived solutes in shallow Archean seawater: rare earth element and Nd isotope evidence in iron formation from the 2.9Ga Pongola Supergroup, South Africa. *Geochimica Cosmochimica Acta* 72, 378–394. doi:10.1016/j.gca.2007.10.028

Ali, K. A., Stern, R. J., Manton, W. I., Johnson, P. R., and Mukherjee, S. K. (2010). Neoproterozoic diamictite in the Eastern Desert of Egypt and northern Saudi Arabia: evidence of ~750 Ma glaciation in the arabian–nubian shield? *Int. J. Earth Sci.* 99, 705–726. doi:10.1007/s00531-009-0427-3

Ali, S., Abart, R., Sayyed, M. I., Hauzenberger, C. A., and Sami, M. (2023). Petrogenesis of the Wadi el-faliq gabbroic intrusion in the central Eastern Desert of Egypt: implications for neoproterozoic post-collisional magmatism associated with the najd fault system. *Minerals* 13, 10. doi:10.3390/min13010010

Alibo, D. S., and Nozaki, Y. (1999). Rare earth elements in seawater: particle association, shale-normalization, and Ce oxidation. *Geochimica Cosmochimica Acta* 63, 363–372. doi:10.1016/s0016-7037(98)00279-8

Angerer, T., Hagemann, S. G., and Danyushevsky, L. V. (2012). Geochemical evolution of the banded iron formation-hosted high-grade iron ore system in the koolyanobbing greenstone belt, western Australia. *Econ. Geol.* 107, 599–644. doi:10.2113/econgeo.107.4.599

Barrett, T. J. (1981). Chemistry and mineralogy of Jurassic bedded chert overlying ophiolites in the North Apennines, Italy. *Chem. Geol.* 34, 289–317. doi:10.1016/0009-2541(81)90118-2

Barrote, V. R., Rosiere, C. A., Rolim, V. K., Santos, J. O. S., and Mcnaughton, N. J. (2017). The Proterozoic Guanhães banded iron formations, Southeastern border of

the São Francisco Craton, Brazil: evidence of detrital contamination. *Geol. Usp. Série Científica* 17, 303–324. doi:10.11606/issn.2316-9095.v17-352

Basta, F. F., Maurice, A. E., Fontboté, L., and Favarger, P.-Y. (2011). Petrology and geochemistry of the banded iron formation (BIF) of Wadi karim and Um Anab, Eastern Desert, Egypt: implications for the origin of neoproterozoic BIF. *Precambrian Res.* 187, 277–292. doi:10.1016/j.precamres.2011.03.011

Bau, M., and Dulski, P. (1996). Distribution of yttrium and rare-earth elements in the penge and kuruman iron-formations, transvaal supergroup, South Africa. *Precambrian Res.* 79, 37–55. doi:10.1016/0301-9268(95)00087-9

Bau, M., and Dulski, P. (1999). Comparing yttrium and rare earths in hydrothermal fluids from the Mid-Atlantic Ridge: implications for Y and REE behaviour during near-vent mixing and for the Y/Ho ratio of Proterozoic seawater. *Chem. Geol.* 155, 77–90. doi:10.1016/s0009-2541(98)00142-9

Bekker, A., Slack, J. F., Planavsky, N., Krapez, B., Hofmann, A., Konhauser, K. O., et al. (2010). Iron Formation: the sedimentary product of a complex interplay among mantle, tectonic, oceanic, and biospheric processes. *Econ. Geol.* 105, 467–508. doi:10.2113/gsecongeo.105.3.467

Bolhar, R., Kamber, B. S., Moorbath, S., Fedo, C. M., and Whitehouse, M. J. (2004). Characterisation of early Archaean chemical sediments by trace element signatures. *Earth Planet. Sci. Lett.* 222, 43–60. doi:10.1016/j.epsl.2004.02.016

Boström, K. (1973). The origin and fate of ferromanganoan active ridge sediments. *Stock. Contributions Geol.* 27, 147–243.

Bruland, K. W. (1989). Complexation of zinc by natural organic ligands in the central North Pacific. *Limnol. Oceanogr.* 34, 269–285. doi:10.4319/lo.1989.34.2.0269

Byrne, R. H., and Kim, K.-H. (1990). Rare earth element scavenging in seawater. *Geochimica Cosmochimica Acta* 54, 2645–2656. doi:10.1016/0016-7037(90)90002-3

Byrne, R. H., and Sholkovitz, E. R. (1996). "Chapter 158 Marine chemistry and geochemistry of the lanthanides," in *Handbook on the Physics and chemistry of rare earths* (Netherlands: Elsevier), 497–593.

Campbell, A. C., Bowers, T. S., Measures, C. I., Falkner, K. K., Khadem, M., and Edmond, J. M. (1988). A time series of vent fluid compositions from 21°N, East Pacific rise (1979, 1981, 1985), and the guaymas basin, gulf of California (1982, 1985). *J. Geophys. Res. Solid Earth* 93, 4537–4549. doi:10.1029/jb093ib05p04537

Chen, J., Algeo, T. J., Zhao, L., Chen, Z.-Q., Cao, L., Zhang, L., et al. (2015). Diagenetic uptake of rare earth elements by bioapatite, with an example from Lower Triassic conodonts of South China. *Earth-Science Rev.* 149, 181–202. doi:10.1016/j.earscirev.2015.01.013

Cox, G. M., Halverson, G. P., Minarik, W. G., Le Heron, D. P., Macdonald, F. A., Bellefroid, E. J., et al. (2013). Neoproterozoic iron formation: an evaluation of its temporal, environmental and tectonic significance. *Chem. Geol.* 362, 232–249. doi:10.1016/j.chemgeo.2013.08.002

Dai, Y., Zhang, L., Wang, C., Liu, L., Cui, M., Zhu, M., et al. (2012). Genetic type, formation age and tectonic setting of the Waitoushan banded iron formation, Benxi, Liaoning Province. *Acta Petrol. Sin.* 28, 3574–3594.

Dalstra, H. J., Rosière, C. A., Hagemann, S., Rosière, C. A., Gutzmer, J., and Beukes, N. J. (2008). "Structural controls on high-grade iron ores hosted by banded iron formation: a global perspective," in *Banded iron formation-related high-grade iron ore* (Shaffer Parkway Littleton, USA: Society of Economic Geologists).

De Baar, H. J. W., German, C. R., Elderfield, H., and Van Gaans, P. (1988). Rare earth element distributions in anoxic waters of the Cariaco Trench. *Geochimica Cosmochimica Acta* 52, 1203–1219. doi:10.1016/0016-7037(88)90275-x

Ding, T., Tan, T., Wang, J., Zhang, C., Ye, X., Liang, J., et al. (2021). Field and zircon U–Pb geochronological evidence for the occurrence of Cambrian banded iron formations in the West Kunlun Orogenic Belt, China. *Gondwana Res.* 98, 1–16. doi:10.1016/j.gr.2021.05.024

Donat, J. R., and Bruland, K. W. (1990). A comparison of two voltammetric techniques for determining zinc speciation in Northeast Pacific Ocean waters. *Mar. Chem.* 28, 301–323. doi:10.1016/0304-4203(90)90050-m

Dunk, R. M., and Mills, R. A. (2006). The impact of oxic alteration on plume-derived transition metals in ridge flank sediments from the East Pacific Rise. *Mar. Geol.* 229, 133–157. doi:10.1016/j.margeo.2006.03.007

Dymek, R. F., and Klein, C. (1988). Chemistry, petrology and origin of banded iron-formation lithologies from the 3800 MA isua supracrustal belt, West Greenland. *Precambrian Res.* 39, 247–302. doi:10.1016/0301-9268(88)90022-8

El Aref, M. M., El Dougdoug, A., Abdel Wahed, M., and El Manawi, A. W. (1993). Diagenetic and metamorphic history of the umm nar BIF, Eastern Desert, Egypt. *Miner. Deposita* 28, 264–278. doi:10.1007/bf02421576

El-Dokouny, H. A., Mahdy, N. M., El Hadek, H. H., Sami, M., Abart, R., Ahmed, M. S., et al. (2023). Origin of amphibole-biotite-fluorite-rich enclaves from gabal el-ineigi fluorite-bearing granite, central Eastern Desert of Egypt: insights into fluoride–calcium and silicate liquid immiscibility. *Minerals* 13, 670. doi:10.3390/min13050670

El-Habaak, G. H. (2021). "Banded iron formation in the Egyptian nubian shield," in *The geology of the Egyptian nubian Shield*. Editors Z. Hamimi, S. Arai, A.-R. Fowler, and M. Z. El-Bialy (Cham: Springer International Publishing), 425–486.

El-Shazly, A. K., and Khalil, K. I. (2016). Metamorphic and geochronologic constraints on the tectonic evolution of the Central Eastern Desert of Egypt. *Precambrian Res.* 283, 144–168. doi:10.1016/j.precamres.2016.07.016

El-Shazly, A. K., Khalil, K. I., and Helba, H. A. (2019). Geochemistry of banded iron formations and their host rocks from the Central Eastern Desert of Egypt: a working genetic model and tectonic implications. *Precambrian Res.* 325, 192–216. doi:10.1016/j.precamres.2019.02.011

Faisal, M., Yang, X., Khalifa, I. H., Amuda, A. K., and Sun, C. (2020). Geochronology and geochemistry of Neoproterozoic Hamamid metavolcanics hosting largest volcanogenic massive sulfide deposits in Eastern Desert of Egypt: implications for petrogenesis and tectonic evolution. *Precambrian Res.* 344, 105751. doi:10.1016/j.precamres.2020.105751

Faisal, M., Yang, X., Zhang, H., Amuda, A. K., Sun, C., Mustafa, S., et al. (2022). Mineralization styles, alteration mineralogy, and sulfur isotope geochemistry of volcanogenic massive sulfide deposits in the Shadli Metavolcanics Belt, South Eastern Desert, Egypt: metallogenic implications. *Ore Geol. Rev.* 140, 104402. doi:10.1016/j.oregeorev.2021.104402

Fawzy, M. M., Mahdy, N. M., and Sami, M. (2020). Mineralogical characterization and physical upgrading of radioactive and rare metal minerals from Wadi Al-Baroud granitic pegmatite at the Central Eastern Desert of Egypt. *Arabian J. Geosciences* 13, 413. doi:10.1007/s12517-020-05381-z

Frei, R., Gaucher, C., Stolper, D., and Canfield, D. E. (2013). Fluctuations in late Neoproterozoic atmospheric oxidation — Cr isotope chemostratigraphy and iron speciation of the late Ediacaran lower Arroyo del Soldado Group (Uruguay). *Gondwana Res.* 23, 797–811. doi:10.1016/j.gr.2012.06.004

German, C. R., Holliday, B. P., and Elderfield, H. (1991). Redox cycling of rare earth elements in the suboxic zone of the Black Sea. *Geochimica Cosmochimica Acta* 55, 3553–3558. doi:10.1016/0016-7037(91)90055-a

Govett, G. J. S. (1966). Origin of banded iron formations. *GSA Bull.* 77, 1191–1212. doi:10.1130/0016-7606(1966)77[1191:oobif]2.0.co;2

Gross, G. (1980). A classification of iron formations based on depositional environments. *Can. Mineralogist* 18, 215–222.

Gutzmer, J., Chisonga, B. C., Beukes, N. J., Mukhopadhyay, J., Hagemann, S., Rosière, C. A., et al. (2008). "The geochemistry of banded iron formation-hosted high-grade hematite-martite iron ores," in *Banded iron formation-related high-grade iron ore* (Shaffer Parkway Littleton, USA: Society of Economic Geologists).

Hallberg, R. (1976). A geochemical method for investigation of palaeoredox conditions in sediments. *Ambio Spec. Rep.* 4, 139–147.

Hou, K., Ma, X., Li, Y., Liu, F., and Han, D. (2019). Genesis of Huoqiu banded iron formation (BIF), southeastern North China Craton, constraints from geochemical and Hf-O-S isotopic characteristics. *J. Geochem. Explor.* 197, 60–69. doi:10.1016/j.gexplo.2018.11.005

Isley, A. E., and Abbott, D. H. (1999). Plume-related mafic volcanism and the deposition of banded iron formation. *J. Geophys. Res. Solid Earth* 104, 15461–15477. doi:10.1029/1999jb900066

Jones, B., and Manning, D. a.C. (1994). Comparison of geochemical indices used for the interpretation of palaeoredox conditions in ancient mudstones. *Chem. Geol.* 111, 111–129. doi:10.1016/0009-2541(94)90085-x

Khalid, A., and Oweiss, K. H. (1997). Results of mineral exploration programs in south eastern Sinai, Egypt. *Ann. Geol. Surv. Egypt* 20, 207–220.

Khalil, K. I., El-Shazly, A. E., and Lehmann, B. (2015). Late Neoproterozoic banded iron formation (BIF) in the central Eastern Desert of Egypt: mineralogical and geochemical implications for the origin of the Gebel El Hadid iron ore deposit. *Ore Geol. Rev.* 69, 380–399. doi:10.1016/j.oregeorev.2015.02.017

Khudeir, A., Ali, M., and El Habaak, G. (1988). The metavolcanics at Um Samiuki area, Egypt. *Bull. Fac. Sci. Assiut Univ.* 17, 73–101.

Kiyokawa, S., Suzuki, T., El-Dokouny, H. A., Dawoud, M., and Abuelhasan, M. M. (2020). Stratigraphy, petrology, and geochemistry of a neoproterozoic banded iron sequence in the El-Dabbah Group, central Eastern Desert, Egypt. *J. Afr. Earth Sci.* 168, 103805. doi:10.1016/j.jafrearsci.2020.103805

Klein, C. (2005). Some Precambrian banded iron-formations (BIFs) from around the world: their age, geologic setting, mineralogy, metamorphism, geochemistry, and origins. *Am. Mineralogist* 90, 1473–1499. doi:10.2138/am.2005.1871

Klein, C., and Beukes, N. J. (1989). Geochemistry and sedimentology of a facies transition from limestone to iron-formation deposition in the early Proterozoic Transvaal Supergroup, South Africa. *Econ. Geol.* 84, 1733–1774. doi:10.2113/gsecongeo.84.7.1733

Klein, C., and Beukes, N. J. (1993). Sedimentology and geochemistry of the glaciogenic late proterozoic rapitan iron-formation in Canada. *Econ. Geol.* 88, 542–565. doi:10.2113/gsecongeo.88.3.542

Li, H., Zhang, Z., Li, L., Zhang, Z., Chen, J., and Yao, T. (2014). Types and general characteristics of the BIF-related iron deposits in China. *Ore Geol. Rev.* 57, 264–287. doi:10.1016/j.oregeorev.2013.09.014

Li, W., Beard, B. L., and Johnson, C. M. (2015). Biologically recycled continental iron is a major component in banded iron formations. *Proc. Natl. Acad. Sci.* 112, 8193–8198. doi:10.1073/pnas.1505515112

Maclean, W. H., and Kranidiotis, P. (1987). Immobile elements as monitors of mass transfer in hydrothermal alteration; Phelps Dodge massive sulfide deposit, Matagami, Quebec. *Econ. Geol.* 82, 951–962. doi:10.2113/gsecongeo.82.4.951

Marchig, V., Gundlach, H., Möller, P., and Schley, F. (1982). Some geochemical indicators for discrimination between diagenetic and hydrothermal metalliferous sediments. *Mar. Geol.* 50, 241–256. doi:10.1016/0025-3227(82)90141-4

Nagarajan, R., Madhavaraju, J., Nagendra, R., Armstrong-Altrin, J. S., and Moutte, J. (2007). Geochemistry of neoproterozoic shales of the rabanpalli formation, bhima basin, northern Karnataka, southern India: implications for provenance and paleoredox conditions. *Rev. Mex. ciencias Geol.* 24, 150–160.

Nath, N. B., Bau, M., Ramalingeswara Rao, B., and Rao, C. M. (1997). Trace and rare earth elemental variation in Arabian Sea sediments through a transect across the oxygen minimum zone. *Geochimica Cosmochimica Acta* 61, 2375–2388. doi:10.1016/s0016-7037(97)00094-x

Ngueutchoua, G., Ngantchu, L. D., Youbi, M., Ngos Iii, S., Beyala, V. K. K., Yifomju, K. P., et al. (2017). Geochemistry of cretaceous mudrocks and sandstones from douala sub-basin, kumba area, south west Cameroon: constraints on provenance, source rock weathering, paleo-oxidation conditions and tectonic environment. *J Int. J. Geosciences* 08 (04), 393–424. doi:10.4236/ijg.2017.84021

Ohta, A., and Kawabe, I. (2001). REE(III) adsorption onto Mn dioxide (δ-MnO2) and Fe oxyhydroxide: Ce(III) oxidation by δ-MnO2. *Geochimica Cosmochimica Acta* 65, 695–703. doi:10.1016/s0016-7037(00)00578-0

Pearce, J. A. (1982). Trace element characteristics of lavas from destructive plate boundaries. *Andesites* 8, 525–548.

Pearce, J. A. (2008). Geochemical fingerprinting of oceanic basalts with applications to ophiolite classification and the search for Archean oceanic crust. *Lithos* 100, 14–48. doi:10.1016/j.lithos.2007.06.016

Pearce, J. A. (2014). Immobile element fingerprinting of ophiolites. *Elements* 10, 101–108. doi:10.2113/gselements.10.2.101

Peng, Z., Wang, C., Poulton, S. W., Tong, X., Konhauser, K. O., and Zhang, L. (2022). Origin of the neoarchean VMS-BIF metallogenic association in the qingyuan greenstone belt, north China craton: constraints from geology, geochemistry, and iron and multiple sulfur (δ33S, δ34S, and δ36S) isotopes. *Econ. Geol.* 117, 1275–1298. doi:10.5382/econgeo.4920

Peter, J. M. (2003). "Ancient iron formations: their genesis and use in the exploration for stratiform base metal sulphide deposits, with examples from the Bathurst Mining Camp," in *Geochemistry of sediments and sedimentary rocks: evolution considerations to mineral deposit-forming environments*. Editor D. R. Lentz (Canada: Geological Association of Canada), 145–176.

Peter, J. M., Goodfellow, W. D., and Doherty, W. (2003). "Hydrothermal sedimentary rocks of the heath steele Belt,Bathurst mining camp, new brunswick: Part 2. Bulk and rare earth element geochemistry and implications for origin," in *Massive sulfide deposits of the bathurst mining camp, new brunswick, and northern Maine*. Editors W. D. Goodfellow, S. R. Mccutcheon, and J. M. Peter (Shaffer Parkway Littleton, USA: Society of Economic Geologists).

Peter, J. M., Leybourne, M. I., Scott, S. D., and Gorton, M. P. (2014). Geochemical constraints on the tectonic setting of basaltic host rocks to the Windy Craggy Cu-Co-Au massive sulphide deposit, northwestern British Columbia. *Int. Geol. Rev.* 56, 1484–1503. doi:10.1080/00206814.2014.947335

Pirajno, F., and Bagas, L. (2008). A review of Australia's Proterozoic mineral systems and genetic models. *Precambrian Res.* 166, 54–80. doi:10.1016/j.precamres.2007.05.008

Pirajno, F., and Yu, H.-C. (2021). Cycles of hydrothermal activity, precipitation of chemical sediments, with special reference to Algoma-type BIF. *Gondwana Res.* 100, 251–260. doi:10.1016/j.gr.2021.02.012

Planavsky, N., Bekker, A., Rouxel, O. J., Kamber, B., Hofmann, A., Knudsen, A., et al. (2010). Rare Earth Element and yttrium compositions of Archean and Paleoproterozoic Fe formations revisited: new perspectives on the significance and mechanisms of deposition. *Geochimica Cosmochimica Acta* 74, 6387–6405. doi:10.1016/j.gca.2010.07.021

Planavsky, N. J., Reinhard, C. T., Wang, X., Thomson, D., Mcgoldrick, P., Rainbird, R. H., et al. (2014). Low Mid-Proterozoic atmospheric oxygen levels and the delayed rise of animals. *Science* 346, 635–638. doi:10.1126/science.1258410

Polat, A., and Frei, R. (2005). The origin of early Archean banded iron formations and of continental crust, Isua, southern West Greenland. *Precambrian Res.* 138, 151–175. doi:10.1016/j.precamres.2005.04.003

Rao, T. G., and Naqvi, S. M. (1995). Geochemistry, depositional environment and tectonic setting of the BIF's of the late archaean chitradurga schist belt, India. *Chem. Geol.* 121, 217–243. doi:10.1016/0009-2541(94)00116-p

Rimmer, S. M. (2004). Geochemical paleoredox indicators in devonian–mississippian black shales, central appalachian basin (USA). *Chem. Geol.* 206, 373–391. doi:10.1016/j.chemgeo.2003.12.029

Robertson, A. H. F., and Hudson, J. D. (1973). Cyprus umbers: chemical precipitates on a Tethyan ocean ridge. *Earth Planet. Sci. Lett.* 18, 93–101. doi:10.1016/0012-821x(73)90039-3

Ross, P. S., and Bédard, J. H. (2009). Magmatic affinity of modern and ancient subalkaline volcanic rocks determined from trace-element discriminant diagrams. *Can. J. Earth Sci.* 46, 823–839. doi:10.1139/e09-054

Roy, S., and Venkatesh, A. S. (2009). Mineralogy and geochemistry of banded iron formation and iron ores from eastern India with implications on their genesis. *J. Earth Syst. Sci.* 118, 619–641. doi:10.1007/s12040-009-0056-z

Said, M., Khalid, A., El Kady, M., Salem, A. A., and Ibrahim, S. (1998). On the structural evolution of banded iron formation of Gabal Kamel and its role in the gold mineralization. *Ann. Geol. Surv. Egypt* 21, 345–352.

Sami, M., Adam, M. M., Lv, X., Lasheen, E. S. R., Ene, A., Zakaly, H. M., et al. (2023a). Petrogenesis and tectonic implications of the cryogenian I-type granodiorites from gabgaba Terrane (NE Sudan). *Minerals* 13, 331. doi:10.3390/min13030331

Sami, M., Azer, M., and Abdel-Karim, A.-A. (2022). Postcollisional ferani volcanics from north arabian–nubian shield (south Sinai, Egypt): petrogenesis and implication for ediacaran (607–593 Ma) geodynamic evolution. *J. Geol.* 130, 475–498. doi:10.1086/724335

Sami, M., Ntaflos, T., Mohamed, H. A., Farahat, E. S., Hauzenberger, C., Mahdy, N. M., et al. (2020). Origin and petrogenetic implications of spessartine garnet in highly-fractionated granite from the central Eastern Desert of Egypt. *Acta Geol. Sin. - Engl. Ed.* 94, 763–776. doi:10.1111/1755-6724.13883

Sami, M., Osman, H., Ahmed, A. F., Zaky, K. S., Abart, R., Sanislav, I. V., et al. (2023b). Magmatic evolution and rare metal mineralization in mount el-sibai peralkaline granites, central Eastern Desert, Egypt: insights from whole-rock geochemistry and mineral chemistry data. *Minerals* 13, 1039. doi:10.3390/min13081039

Simonson, B. M. (1985). Sedimentological constraints on the origins of Precambrian iron-formations. *GSA Bull.* 96, 244–252. doi:10.1130/0016-7606(1985)96<244:scotoo>2.0.co;2

Soh Tamehe, L., Nzepang Tankwa, M., Chongtao, W., Ganno, S., Ngnotue, T., Kouankap Nono, G. D., et al. (2018). Geology and geochemical constrains on the origin and depositional setting of the Kpwa–Atog Boga banded iron formations (BIFs), northwestern Congo craton, southern Cameroon. *Ore Geol. Rev.* 95, 620–638. doi:10.1016/j.oregeorev.2018.03.017

Stacey, J. S., Doe, B. R., Roberts, R. J., Delevaux, M. H., and Gramlich, J. W. (1980). A lead isotope study of mineralization in the Saudi Arabian Shield. *Contributions Mineralogy Petrology* 74, 175–188. doi:10.1007/bf01132003

Stern, R. J., and Abdelsalam, M. G. (1998). Formation of juvenile continental crust in the Arabian–Nubian shield: evidence from granitic rocks of the Nakasib suture, NE Sudan. *Geol. Rundsch.* 87, 150–160. doi:10.1007/s005310050196

Stern, R. J., Avigad, D., Miller, N. R., and Beyth, M. (2006). Evidence for the Snowball earth hypothesis in the arabian-nubian shield and the East African orogen. *J. Afr. Earth Sci.* 44, 1–20. doi:10.1016/j.jafrearsci.2005.10.003

Stern, R. J., and Hedge, C. E. (1985). Geochronologic and isotopic constraints on late precambrian crustal evolution in the Eastern Desert of Egypt. *Am. J. Sci.* 285, 97–127. doi:10.2475/ajs.285.2.97

Stern, R. J., Mukherjee, S. K., Miller, N. R., Ali, K., and Johnson, P. R. (2013). ~750Ma banded iron formation from the Arabian-Nubian Shield—implications for understanding neoproterozoic tectonics, volcanism, and climate change. *Precambrian Res.* 239, 79–94. doi:10.1016/j.precamres.2013.07.015

Stoffers, P., Glasby, G. P., Stuben, D., Renner, R. M., Pierre, T. G., Webb, J., et al. (1993). Comparative mineralogy and geochemistry of hydrothermal iron-rich crusts from the Pitcairn, Teahitia-mehetia, and MacDonald hot spot areas of the S. W. pacific. *Mar. Georesources Geotechnol.* 11, 45–86. doi:10.1080/10641199309379905

Sun, S. S., and Mcdonough, W. F. (1989). *Chemical and isotopic systematics of oceanic basalts: implications for mantle composition and processes*. London: Geological Society, 313–345.

Sylvestre, G., Evine Laure, N. T., Gus Djibril, K. N., Arlette, D. S., Cyriel, M., Timoléon, N., et al. (2017). A mixed seawater and hydrothermal origin of superior-type banded iron formation (BIF)-hosted Kouambo iron deposit, Palaeoproterozoic Nyong series, Southwestern Cameroon: constraints from petrography and geochemistry. *Ore Geol. Rev.* 80, 860–875. doi:10.1016/j.oregeorev.2016.08.021

Taner, M. F., and Chemam, M. (2015). Algoma-type banded iron formation (BIF), Abitibi Greenstone belt, Quebec, Canada. *Ore Geol. Rev.* 70, 31–46. doi:10.1016/j.oregeorev.2015.03.016

Taylor, S. R., and Mclennan, S. M. (1985). *The continental crust, its composition and evolution: an examination of the geochemical record preserved in sedimentary rocks*. Oxford; Boston: Blackwell Scientific.

Thurston, P. C., Kamber, B. S., and Whitehouse, M. (2012). Archean cherts in banded iron formation: insight into Neoarchean ocean chemistry and depositional processes. *Precambrian Res.* 214-215, 227–257. doi:10.1016/j.precamres.2012.04.004

Tostevin, R., Wood, R. A., Shields, G. A., Poulton, S. W., Guilbaud, R., Bowyer, F., et al. (2016). Low-oxygen waters limited habitable space for early animals. *Nat. Commun.* 7, 12818. doi:10.1038/ncomms12818

Toth, J. R. (1980). Deposition of submarine crusts rich in manganese and iron. *GSA Bull.* 91, 44–54. doi:10.1130/0016-7606(1980)91<44:doscri>2.0.co;2

Usma, C. D., Sial, A. N., Ferreira, V. P., Gaucher, C., and Frei, R. (2021). Ediacaran banded iron formations and carbonates of the Cachoeirinha Group of NE Brazil: paleoenvironment and paleoredox conditions. *J. S. Am. Earth Sci.* 109, 103282. doi:10.1016/j.jsames.2021.103282

Wang, X., Lv, X., Cao, X., Yuan, Q., Wang, Y., Liu, W., et al. (2016). Petrology and geochemistry of the banded iron formation of the kuluketage block, xinjiang, NW China: implication for BIF depositional setting. *Resour. Geol.* 66, 313–334. doi:10.1111/rge.12107

White, W. M. (2013). *Geochemistry*. Oxford: Wiley-Blackwell.

Winchester, J. A., and Floyd, P. A. (1977). Geochemical discrimination of different magma series and their differentiation products using immobile elements. *Chem. Geol.* 20, 325–343. doi:10.1016/0009-2541(77)90057-2

Wright, J., Schrader, H., and Holser, W. T. (1987). Paleoredox variations in ancient oceans recorded by rare earth elements in fossil apatite. *Geochimica Cosmochimica Acta* 51, 631–644. doi:10.1016/0016-7037(87)90075-5

Zartman, R. E., and Doe, B. R. (1981). Plumbotectonics—the model. *Tectonophysics* 75, 135–162. doi:10.1016/0040-1951(81)90213-4

Zhang, X., Zhang, L., Xiang, P., Wan, B., and Pirajno, F. (2011). Zircon U–Pb age, Hf isotopes and geochemistry of Shuichang Algoma-type banded iron-formation, North China Craton: constraints on the ore-forming age and tectonic setting. *Gondwana Res.* 20, 137–148. doi:10.1016/j.gr.2011.02.008

Zhou, Z., Zhu, X., Sun, J., Li, Z., and Chen, S. (2024). Large-scale Mesoproterozoic iron formations in northwestern China. *Precambrian Res.* 400, 107243. doi:10.1016/j.precamres.2023.107243